Eur. J. Mech. B - Fluids 19 (2000) 173–211

S0997-7546(00)00107-2/FLA

Nonlinear effects in absolute and convective instabilities of a near-wake

Frank T. Smith, Rowena G.A. Bowles, Linzhong Li

Department of Mathematics, University College London, Gower Street, London WC1E 6BT, UK

(Received 7 May 1998; revised 23 July 1999; accepted 7 October 1999)

Abstract – Linear and nonlinear initial-value problems are discussed for planar inviscid disturbances in streamlined near-wakes. This is mostly for those areas of near-wake flow where the basic motion comprises nearly uniform shear with or without normal influx into the accompanying viscous interfacial layer, although agreement is found with linear properties for full velocity profiles of double-Blasius, double-Jobe–Burggraf, Hakkinen–Rott and Goldstein form. With nonlinear disturbances, wavelike initial conditions yield a known critical-layer development, whereas more general, non-wave, initial conditions lead to a new integro-partial-differential amplitude equation which is studied analytically and numerically. The solutions show decay, finite-time blowup or nonlinear upstream-travelling disturbances. The normal influx proves crucial. Absolute and upstream- or downstream-convective instability is encountered (depending on the profiles, and flow reversal, for example); and in generic cases (for any thin airfoil) nonlinearity is shown analytically to provoke upstream convection. Increased nonlinearity drives the typical transition point extremely close to the trailing edge. Comparisons are made with three-dimensional behaviour in the linear case and with a direct simulation in the nonlinear regime. © 2000 Éditions scientifiques et médicales Elsevier SAS

1. Introduction

Linear and nonlinear disturbance growth in the thin wake behind a streamlined body is the prime concern here, especially within the near-wake region just aft of a trailing edge. There have been numerous theoretical investigations of classical type for temporal or spatial instability in wakes, as described by Drazin and Howard [1], Mattingly and Criminale [2], Drazin and Reid [3], Papageorgiou and Smith [4], Woodley and Peake [5] and references therein, including a number of comparisons with experiments such as those in Sato and Kuriki [6], Mattingly and Criminale [2]], Miksad et al. [7,8], Papageorgiou and Smith [4]. The interest in this study, however, especially concerns the linear and subsequent nonlinear disturbance development from a general initial value. Ideas and recent theoretical/numerical works on linear absolute and convective instability (Briggs–Bers) are therefore of relevance initially, including those by Gaster [9–11], Huerre and Monkewitz [12], Monkewitz, Huerre and Chomaz [13], Allen and Riley [14], Lingwood [15], Woodley and Peake [5] for viscous or inviscid disturbances in different contexts of boundary layers, free shear layers and wakes, mostly of developed form; see also Drazin [16], Le Dizès et al. [17]. Many of the above investigations work at finite Reynolds numbers, using numerical solutions with various approximations. There appears to be little existing investigation on more analytical or explicit features, on flow structure, or on precise calculation of nonlinear effects, in wakes, for general initial-value problems; compare the nonlinear studies by Papageorgiou and Smith [18], Goldstein and Hultgren [19], Goldstein and Choi [20,21] and others on disturbances of fixed or restricted wavelength or frequency, and the direct numerical simulations of Hannemann and Oertel [22] (see also Jackson [23]) for unsteady flow past a thin non-streamlined body. Relatively little attention has been paid also to the significant area of near-wakes, where much of the fluid motion is un-developed as well as relatively complex. There is in particular an interesting gap to be considered concerning the nonlinear evolution of disturbances especially in near wakes, given moreover that the rest of the wake may be dependent on the near-wake properties.

The need to find more explicitly the dependence of an evolving disturbance in the wake on the initial state and on the local wake velocity profiles, whether generic or not, suggests a more analytical and rational approach may be fruitful. That alternative is pursued here. A simple point made by Papageorgiou and Smith [4], and re-emphasized by Woodley and Peake [5], is that wake-instability calculations should be based on genuine wake-velocity profiles (starting, in the case of a full wake for example, from a double-Blasius-like form just after the trailing edge) rather than the typical model profiles often assumed (e.g., tanh-squared and other developed forms), and the same point applies to other settings such as in free shear layers. Likewise many approximations made at finite Reynolds numbers do not strictly have a rational basis, even if they may have some intuitive physical validity. It seems clear from the above that the near-wake response, with its un-developed profiles, is worth studying first, at large Reynolds numbers.

The near wake is often taken to refer specifically to the start (Goldstein [24]) of the full classical wake behind an airfoil, governed by the boundary-layer equations with prescribed pressure gradient, but it can refer also to elsewhere in the complex local flow, including the start (Hakkinen and Rott [25]) of the interactive wake on a shorter scale inside the triple-deck structure, with pressure-displacement interaction controlling the basic flow in the lower-deck sublayer; there the main wake effects enter play (Stewartson [26], Messiter [27], Jobe and Burggraf [28], Chow and Melnik [29], Veldman and van de Vooren [30], Smith [31]). A gentle reminder of the near-wake flow structure is presented in *figure 1*. In that sublayer the farfield conditions are those of uniform shear motion instead of the uniform velocities appropriate to the start of the full wake. The property that neither the Hakkinen–Rott nor the Goldstein solution exhibits inflectional velocity profiles then begs the question of where inviscid/inflectional instability starts, in a basic symmetric wake. For the flow past an aligned flat-plate trailing edge the inflection point, which one might associate with inviscid instability, originates just outside the tiny inflection-free region of nonparallel motion where the Navier–Stokes equations apply in full, buried inside the triple-deck structure (see *figure 1*(*a*)); then it emerges close to the Hakkinen–Rott near-wake layer and it travels downstream inside the lower-deck sublayer motion until, at a finite station (as inflection disappears in the local velocity profile), it migrates normally towards the main deck. The inflection point subsequently enters the full wake just outside the Goldstein near-wake layer. For other trailing-edge configurations the inflection point may or may not accompany closely the Hakkinen–Rott near-wake, depending on the velocity profiles sweeping off the upper and lower trailing edges.

In all streamlined configurations, most of the near-wake in effect contains an interface, the exceptions being within a sufficiently thin viscous sublayer such as the Hakkinen–Rott, the lower-deck or the Goldstein layer. The Hakkinen–Rott case, we note, yields an influx normal velocity at its outer edge, a factor which turns out to be important for its stability. The different configurations, and the roles of the inflection point(s) and profile curvatures locally, are to be investigated here. The current investigation in fact holds for almost all senses of the near-wake, including those of Goldstein and Hakkinen–Rott. The present authors' initial interest arose partly from studies of flows past multiple blades, where numerous types of near wake can occur even over the length scale of an entire blade (Smith and Timoshin [32,33], Bowles and Smith [34]) and several distinct kinds of profile distortion from the state of uniform shear mentioned earlier are found to appear in the near-wake flow solutions, due to thickness or camber of the blades. In certain cases such as for short wakes between blades, for long blades, or for many blades, the whole wake from one trailing edge to the succeeding leading edge is of near-wake, undeveloped, form.

The feature that near-wakes may involve significant disturbance activity close to the wake centre-line (interface), where the two flows of vorticity with opposite sign sweep off the upper and lower trailing edges and interact, provides other motivations for this study. Works by Dritschel [35,36], Pullin et al. [37], Clarke and Johnson [38,39] and others consider the nonlinear inviscid development of interacting flows with piecewise uniform vorticity (and related quantities) typically in the context of modelling turbulent flow structures (see

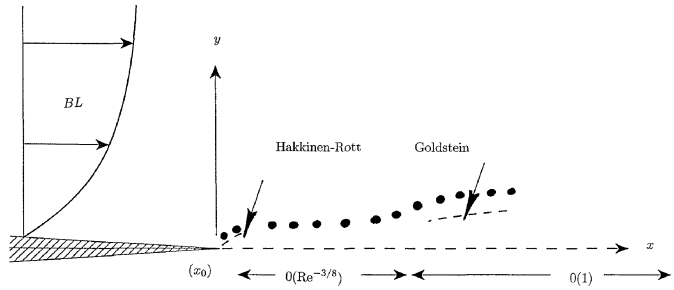

(a)

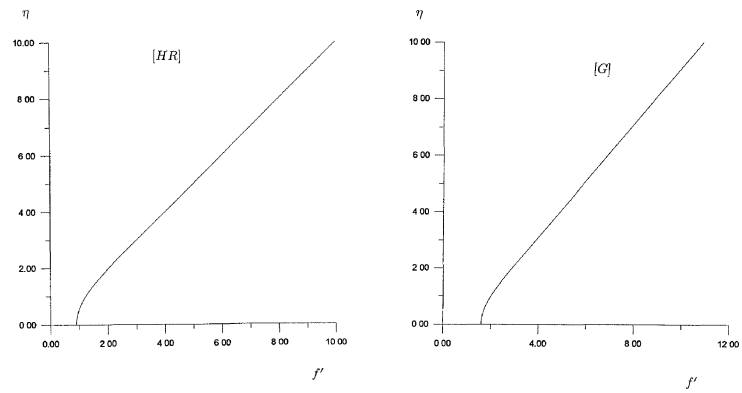

(b)

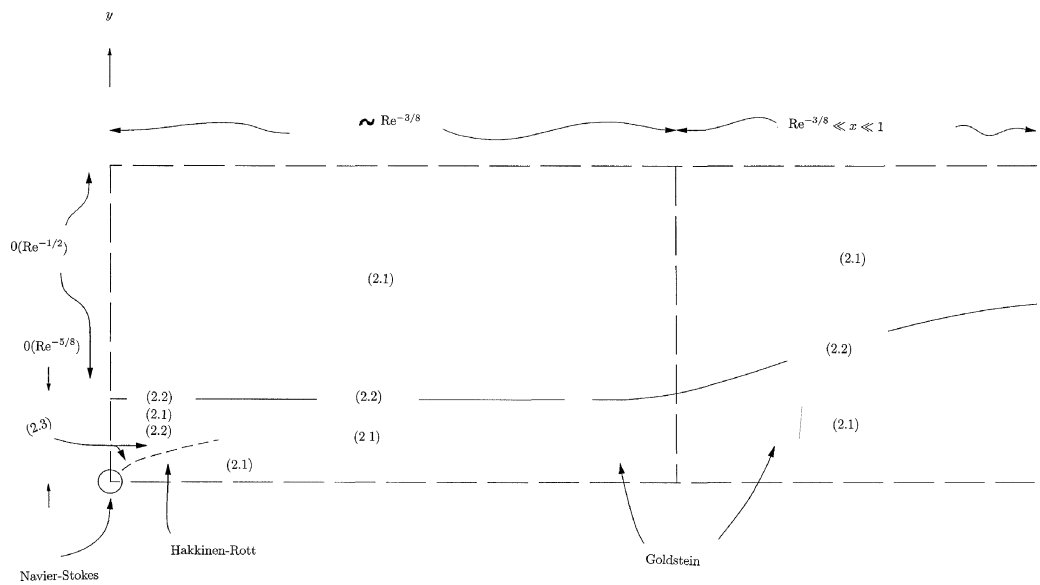

(c)

Figure 1. The local flow. (a) Basic motion, as the incident boundary layer BL (e.g. Blasius) sweeps past the trailing edge $x = 0$, inducing the Hakkinen–Rott near-wake, then the lower-deck sublayer and then the Goldstein near-wake; small circles indicate approximate positions of the inflection points for sufficiently thin airfoils such as the aligned flat plate. (b) Hakkinen–Rott and Goldstein profiles from (4a–c). (c) The areas of application of the basic flows (1)–(3) (see section 2), for the near-wake of an aligned flat plate.

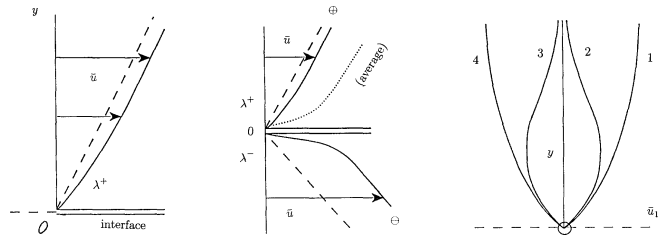

Figure 1. (Continued) (d) For (2), symmetric cases ($\lambda^+ = -\lambda^-$) near the interface containing the viscous layer. (e) Nonsymmetric cases, showing the averaging process (Sections 3.2 and 3.3). (f) Examples of $\bar{u}_1(y)$ profiles, 1 being unstable, 2 and 3 unstable-stable, 4 stable. The cases in (d), (e) are unstable ($\bar{u}_1'' < 0$), corresponding to a favourable pressure gradient upstream.

also Kawahara et al. [40]) and certain geophysical motions. Numerical time-marching approaches with contour dynamics are generally used, showing so-called filaments or squirts of vorticity from the evolving interface among other interesting nonlinear phenomena. The influence on these models from continuous non-uniform vorticity (cf. Dritschel [36]), however small, is considered to be of interest. There is possible impact intended also here on separating flows and free shear layers.

Given the main focus on near-wakes, with significant velocity profile distortions from the trailing edge, whether symmetric or not, the typical input velocity profile $\bar{u}$ considered herein is continuous but with different shear values just on either side of the interface; reversed flow is allowed, for instance. In nonsymmetric cases such as in Smith [31], Bowles and Smith [34] where one-sided separation may occur on the airfoil or blade upstream, viscous effects force reattachment to occur before the trailing edge, leaving forward basic flow near the interface, whereas symmetric cases with upstream separation taking place tend to leave reversed basic flow near the interface. In either case with unsteady disturbances present, this interface, containing the near-wake viscous layer of Hakkinen–Rott, Goldstein or in-between sublayer form, evolves with its position unknown and with effectively zero thickness, in the present inviscid formulation on short scales. The flow is taken to be two-dimensional, in line with comments by Papageorgiou and Smith [4,18] on experiments in the near-wake, and the fluid is taken to be incompressible of constant density ρ. The profile $\bar{u}$ depends on the length scales examined, corresponding to those of the input disturbance, so that $\bar{u}$ can be, for instance, a profile of double-Blasius or double-Jobe–Burggraf form with an interface, the smooth profile of Hakkinen–Rott or Goldstein with no interface, or of nearly linear form in the areas between. More generally $\bar{u}$ gives concentrated, continuous, non-uniform vorticity usually, as in the velocity profiles found in trailing-edge flow studies above for multiple-blade or condensed geometries for example. Our concern is particularly with the effects of that continuous vorticity non-uniformity, of the influx velocity mentioned earlier and of nonlinearity. Without those effects, the near-wake (which is often the first area beyond the trailing edge at which inviscid instability arises, as in the onsets addressed by Savin [41], Smith [42]) mostly yields a response of fixed frequency in time (t_D) for any disturbances concentrated near the interface; the response is specifically of the form $\exp(\pm\frac{1}{2}i[\partial u_D/\partial y_D]t_D)$ regardless of the wavenumber, as in Papageorgiou and Smith [4] and in limits of previous analyses, and so the disturbance is not convected upstream or downstream. Here the subscript D denotes dimensional quantities and the square brackets signify the input jump in shear across the interface. In the presence of influx, small non-uniform vorticity and/or nonlinearity the above fixed-frequency result is altered only slightly at first, this providing the starting point for the current discussion of linear and nonlinear instability locally aimed at more analytical understanding. The non-uniform vorticity and/or nonlinearity above in particular are found to induce typical disturbance growths much larger than those of the double Blasius form (in Papageorgiou and Smith [4]), albeit over shorter scales, and also show analytically a strong destabilising influence from negative values of

the input profile curvature as distinct from the influence of positive curvature characteristic of wall-bounded flows (e.g., ahead of the trailing edge). It is interesting to find that, in a sense, a stable velocity profile on the surface upstream of a trailing edge becomes unstable immediately in the near-wake, and vice-versa.

The velocity components u, v, pressure p, Cartesian coordinates x, y and time t used below for the base flow are nondimensionalised with respect to the representative freestream velocity $\overline{u_\infty}$, the airfoil or blade chord $\overline{\ell_\infty}$, and ρ, the Reynolds number Re being $\overline{u_\infty}\,\overline{\ell_\infty}/\bar{\upsilon}$ where $\bar{\upsilon}$ is the kinematic viscocity of the fluid. To simplify the notation a further scaling will be assumed as the disturbance theory progresses, however, to accommodate the different normal widths ℓ_∞ typical of the distinct areas of the near-wake motion, hinted at earlier, as the incident velocity profiles stream from the trailing edge into the near-wake. The width ℓ_∞ and the corresponding representative velocity u_∞ are assumed to be of the same order as or small compared with the full boundary-layer thickness and the free-stream velocity (see *figure 1*(*a*)–(*c*)), respectively, an assumption which is clearly valid for the Hakkinen–Rott parts of the near-wake as well as for the lower-deck sublayer and Goldstein settings. The coordinates are body-fixed and aligned such that the undisturbed wake occupies $y = 0$ for $x > 0$, where $x = 0$ gives the trailing-edge station. In the ensuing local stability analysis near a downstream station $x_0(> 0)$ the ratio of x_0 to the characteristic $|y|$ scale ℓ_∞ is usually taken to be large.

Section 2 summarizes the basic flow properties in the streamlined near-wake. Three characteristic forms are observed in different regions, to the required order, (a) a full streamwise profile $\bar{u}(y)$ in effect, (b) a near-uniform shear $|y| + \varepsilon\bar{u}_1(y)$, and (c) a uniform shear $|y|$ allied with a normal influx velocity of order ε at the interface, taking account of the ℓ_∞, u_∞ factors, with ε being a given small parameter in (b), (c) and the distortion profile $\bar{u}_1(y)$ in (b) usually smooth of order unity; see *figure 1*(*a*)–(*f*). Numerous different examples of symmetric and nonsymmetric near-wake profiles are in the viscous-inviscid studies of Chow and Melnik [29], Smith [31], Elliott and Smith [43], Bowles and Smith [34], and of references therein, allowing for condensed-geometry flows and various surface distortions upstream.

Section 3 considers planar linear instabilities of (a)–(c) according to the Rayleigh equation, for guidance (the three-dimensional case is in Appendix A), beginning with results for the Hakkinen–Rott, Goldstein, double-sublayer and double-Blasius profiles as in (a). The Hakkinen–Rott and Goldstein cases are without interfaces of course. This is followed by analysis, and then large-time implications, including the issue of absolute and convective instability, for (b), (c). (Comparisons between the analysis and the computations are found to be close at ε values up to about 0.5.) The destabilising role of negative curvature values ($\bar{u}_1'' < 0$), which is in keeping with the inflection point implied then by the positive curvature of the Hakkinen–Rott or Goldstein thin-layer profile, is highlighted along with the explicit roles of the quantity $|y|\bar{u}_1''$ for the symmetric case and the average $|y|[(\bar{u}_1'')^+ + (\bar{u}_1'')^-]/2$ for the nonsymmetric case in determining the temporal growth rates. Particular examples show absolute instability (in some model cases, Appendix B, or with reversed flow), based on examination of the group velocity and the method of steepest descents, or low-speed convective instability (for many cases including those examined in (a) above); this all depends on the precise profile curvature. As the cases (b), (c) (cf. Hocking [44]) are clearer for analysing and understanding initial-value dependence and nonlinear effects, the rest of the paper is on those cases. The properties in Section 3 in fact also provide the ideas on the main scales, flow structure and on nonlinearity pursued subsequently, two temporal scales being found relevant. Thus Section 4 re-examines the first temporal stage, in real space, to help understand how nonlinear effects enter, as well as verifying, together with Sections 5, 6, the results of Section 3 for the linear regime and the absence of spatial growth or decay at leading order. The initial conditions here have the perturbations to the vorticity and to the interface shape being zero or small, cf. Stewartson [45,46]. Transient behaviour which is observed in the analysis of Section 4 plays little part in the linear or nonlinear dynamics of the second temporal stage. The latter stage, with nonlinearity, is described in Sections 5, 6, the type of nonlinearity induced being dependent on the type of initial input disturbance. Wave-like input yields first nonlinear responses within critical

layers, as considered in Section 5, responses which reduce (whether for a single wave or multiple waves) to a single problem that has been much studied previously and indicates nonlinear saturation. By contrast, more general non-wave-like input leads to a more global, sensitive, nonlinear response, at higher amplitudes, which is studied in Section 6 analytically and computationally. There all wavenumber components are agitated in effect. The solutions illustrate finite-time blow-up, nonlinear travelling waves or disturbance decay as the main outcomes, but with evidence of low-speed upstream convection of the nonlinear disturbances. The nonlinear effects of the normal influx and initial conditions are crucial, rather than the shear distortion. Further comments are made in Section 7; these are for example on the properties of linear and nonlinear evolution and on the sensitivity of constant-vorticity computations to small non-uniformities in the vorticity; the presence of upstream-convecting disturbances nonlinearly; their absence and that of absolute instability linearly, for the pure flat-plate motion; the presence (in contrast) of linear absolute and upstream-convecting instability in more distorted near-wakes; and comparisons with direct numerical simulations.

2. Basic flow

Our concern is with the flow in near wakes, which have an involved structure. Nevertheless the basic steady motion (u, v) there can be regarded rationally, for the purposes of the subsequent inviscid disturbance analysis, as providing either a quasi-parallel full, nontrivial, velocity profile $\bar{u}(y)$, so that

$$(u, v) = \big(\bar{u}(y), 0\big) \tag{1}$$

in effect, or a nearly uniform shear flow such that

$$(u, v) = \big(\pm y + \varepsilon\bar{u}_1(y), 0\big), \tag{2}$$

or

$$(u, v) = (\pm y, \mp\varepsilon B). \tag{3}$$

Here (1)–(3) all hold to within a multiplicative constant which does not affect their instability properties. The parameter ε in cases (2) and (3) is small and positive, the distortion $\bar{u}_1(y)$ giving nonzero profile curvature, while the term B is a positive constant due to the viscous Hakkinen–Rott influx velocity (variously described as the suction, entrainment or mass flux into the Hakkinen–Rott layer), and $y \gtrless 0$ respectively. The basic motion close to a typical station $x = x_0 > 0$ is considered, where inviscid instability arguments point to a corresponding local y scale of order $|x - x_0|$, essentially because of Laplacian properties. The direct influence of the trailing-edge geometry itself is expected to be negligible provided that the limitation $|y| \ll x_0$, of slenderness, is satisfied.

Examples of (1)–(3) are given in recent blade-wake flow studies (Smith and Timoshin [32,33], Bowles and Smith [34]) as well as in earlier trailing-edge flow calculations (Jobe and Burggraf [28], Melnik and Chow [29], Smith [42]). Full profiles (1) are obtained in the lower-deck sublayer, in condensed-flow sublayers, in double-Blasius areas and further downstream. Cases (2) of near-uniform vorticity are found in condensed flows with sufficiently small thickness or camber, for instance, as well as in analogues of flows in the following paragraph. Cases (3) of uniform shear and normal influx are virtually omni-present very close to the trailing edge as described below.

The near-wake of an aligned finite flat plate, a central case much studied, yields (1)–(3) in detail as shown schematically in *figure 1*(*c*). Thus (1) applies first for stations $Re^{-3/4} \ll x_0 \ll Re^{-3/8}$ with $Re^{1/8}\bar{u}(y)$ being the

Jobe–Burggraf profiles at the trailing edge, in $y \gtrless 0$ where $|y|$ is of order $Re^{-5/8}$, coupled with an interface effect. These scales are based on the well-established trailing-edge flow structure consisting of the $O(Re^{-3/8})$ long triple-deck (with $|y|$ scales of order Re^{-m}, $m = 3/8, 1/2, 5/8$) and the tiny Navier–Stokes region where $x_0, |y|$ are both of $O(Re^{-3/4})$. There is an interesting staircase structure at higher order (Veldman [47]) but it has negligible impact on what follows. The form (1) also holds for the double-Blasius area where $\bar{u}$ is $O(1)$, $|y| \sim Re^{-1/2}$ and $Re^{-1/2} \ll x_0 \ll 1$, the lower restriction here again limiting the influence of the trailing edge, and an interface again being present astride $y = 0$; the rest of the wake downstream where $x_0 \sim 1$ likewise gives (1). Profiles (1) hold further throughout $|y| \sim Re^{-5/8}$, with $O(Re^{-3/8}) \leqslant x_0 \ll 1$, as smooth lower-deck profiles with $\bar{u}$ of order $Re^{-1/8}$. Finally (1) applies for the smooth similarity profiles of Hakkinen and Rott [25] and Goldstein [24], both of which have $|y| \sim Re^{-1/2}x_0^{1/3}$ and

$$\bar{u} = x_0^{1/3}\bar{f}'(\bar{\eta}), \qquad \bar{\eta} \equiv Re^{1/2}y/x_0^{1/3},$$
$$\bar{f}''' + \frac{2}{3}\bar{f}\bar{f}'' - \frac{1}{3}\bar{f}'^2 = \frac{2}{3}\pi_1, \tag{4a, b, c}$$

with $\bar{f}(0) = \bar{f}''(0) = 0$ and π_1 being a basic pressure-gradient parameter (the basic scaled pressure is of the form $\bar{p}(0) + \pi_1 x_0^{2/3}$ locally). Here the Hakkinen–Rott solution is for the range $Re^{-3/4} \leqslant x_0 \ll Re^{-3/8}$, lying between the triple-deck and Navier–Stokes regions, and has $\bar{f} \sim \frac{1}{2}\lambda(\bar{\eta} + b)^2 + \pi_1/\lambda$ as $\bar{\eta} \to \infty$, where λ denotes the Jobe–Burggraf scaled surface-shear value, b is required to be zero, as in condensed flows, and $\pi_1 > 0$; whereas the Goldstein form covers the further downstream range $Re^{-3/8} \ll x_0 \ll 1$, with λ denoting the Blasius surface-shear value, π_1 required to be zero and $b < 0$; see *figure 1*(*b*), (*c*). Second here, cases (2) hold in the areas between the Hakkinen–Rott and the Jobe–Burggraf solutions, between the lower and main decks, and between the Goldstein and double-Blasius profiles. These again are as marked in *figure 1*(*c*) (see also *figure 1*(*d*)–(*f*)), and are in addition to the examples noted in the previous paragraph. Third, cases (3) apply in an area relatively near the trailing edge as shown in *figure 1*(*c*), between the Hakkinen–Rott and Jobe–Burggraf profiles and between the triple-deck and Navier–Stokes regions. The restrictions on (3) therefore include

$$Re^{-1/2}x_0^{1/3} \ll |y| \ll Re^{-5/8}, \qquad Re^{-3/4} \ll x_0 \ll Re^{-3/8}, \tag{5a, b}$$

and are completed by

$$|y| \ll x_0, \qquad |y| \ll Re^{-13/16}x_0^{-1/6}. \tag{5c, d}$$

Here (5c) is from the limitation explained after (3). Also, (5d) stems from the requirement that the normal inertial operator $v\partial/\partial y$ should exceed, in magnitude, the streamwise operator $Re^{9/8}y^2\partial/\partial x$ due to the local distortion $\varepsilon\bar{u}_1$ effectively being $Re^{-1/8}\lambda_2(Re^{5/8}y)^2$, where $\lambda_2 \sim 1$ is the surface curvature of the Jobe–Burggraf profile at the trailing edge. (The distortion from λ_2 is greater than the distortion of relative order $Re^{1/4}x_0^{2/3}$ from $Re^{3/8}x_0$ being small and positive in the wake: see the local expansions in Stewartson [26].) Since again $|y| \sim |x - x_0|$ is expected in the disturbance behaviour, and since v has the influx value $-(2\pi_1/3\lambda)Re^{-1/2}x_0^{-1/3}$ (< 0) from (4a–c), at large positive $\bar{\eta}$, the restriction (5d) is obtained. The streamwise interval (x_0) of application for the case (3) therefore lies between $O(Re^{-3/4})$ and $O(Re^{-5/8})$, in view of (5a–d). This last case (3) arises because of the zero-b (zero displacement) condition on (4a–c) in the Hakkinen–Rott flow, unlike in the Goldstein solution. Moreover, the influx term $B = (2\pi_1/3\lambda)[\propto \bar{p}'(x_0)/\lambda]$ then is positive and $O(1)$, corresponding to the exact basic-flow solution $u = \lambda y$, $v = -\bar{p}'/\lambda$ of the boundary-layer equations at the edge of the Hakkinen–Rott layer. In a sense, (3) is the most generic of the cases.

Combinations of (2), (3) hold also. One, again generic, is for $|y| \sim Re^{-13/16}x_0^{-1/6}$ where, in view of (5d), (u, v) has the form $(\pm y + \varepsilon\bar{u}_1(y), \mp\varepsilon B)$ with $\bar{u}_1$ then being $\lambda_2 y^2$ effectively, yielding negative profile curvature

if $\lambda_2 > 0$. Another generic case has the same form but with $\bar{u}_1$ exponential in y, holding just (logarithmically) outside the Hakkinen–Rott layer (cf. (5a)) in view of the decay of $(\bar{f}' - \lambda\bar{\eta})$ at large $|\bar{\eta}|$ in (4c), this yielding positive profile curvature. On the other hand, there appears to be no region of the near-wake where all three contributions, due to these two $\bar{u}_1$ forms and to B, are equally important.

Unsteady disturbances will be examined next, initiated with their length scales equal to those of the basic-flow areas where, in *figure 1*(*c*), (1)–(3) apply in turn.

3. Properties from Rayleigh's equation

The following properties act as guides to the evolving flow structure in the near-wake, the length, time and velocity scales now being based on ℓ_∞, u_∞. Solutions of the Rayleigh equation are derived computationally in Subsection 3.1 for full profiles (1), and analytically in Subsection 3.2 for (2) and (3), and then specific examples are considered in Subsection 3.3. Henceforth the coordinate x stands for the original $(x - x_0)$ and so remains a body-fixed coordinate. A linear disturbance $\propto \exp(i\alpha(x - ct)) + \text{CC}$ with wavenumber α (real or complex) and wavespeed c is governed formally by the Rayleigh equation for the disturbance stream function $\tilde{\psi}(y)$,

$$(\bar{u} - c)(\tilde{\psi}'' - \alpha^2\tilde{\psi}) = \bar{u}''\tilde{\psi}, \tag{6a}$$

subject to the boundary conditions

$$\tilde{\psi} \to 0 \quad \text{as } y \to \pm\infty. \tag{6b}$$

The conditions (if any) at zero y vary from case to case; thus for the smooth symmetric Hakkinen–Rott and Goldstein cases we may impose

$$\tilde{\psi}' = 0 \quad \text{at } y = 0, \tag{6c}$$

assuming sinuous modes; whereas for the interfaces which are present in many near-wake areas we have, across $y = 0$,

$$\begin{aligned} \tilde{\psi}^+ = \tilde{\psi}^-, \qquad & [c - \bar{u}(0)](\tilde{\psi}^+)' + \lambda^+\tilde{\psi}^+ + \varepsilon B(\tilde{\psi}^+)''/(i\alpha) \\ & = [c - \bar{u}(0)](\tilde{\psi}^-)' + \lambda^-\tilde{\psi}^- - \varepsilon B(\tilde{\psi}^-)''/(i\alpha) \end{aligned} \tag{6d, e}$$

on inviscid grounds, for the full basic-flow profiles $\bar{u}(y)$ specified as in (1); see *figure 1*. The influx term in B is displayed for the sake of the case (3) and later, B being zero for cases (1) and (2). Also, CC signifies the complex conjugate, a prime denotes a y-derivative, and $+, -$ signs apply respectively to the flow regions $y > 0$, $y < 0$, while $\lambda^\pm$ denote $\bar{u}'(0\pm)$. The condition (6c) which applies for the smooth Hakkinen–Rott and Goldstein cases for example is equivalent to $\lambda^\pm$ being zero and, to repeat, corresponds to a sinuous mode with $\tilde{\psi}$ being even in y. The constraints (6d,e), for the double-Blasius and double-Jobe–Burggraf cases among many others, are implied by continuity of normal velocity and pressure across the interface centred along $y = 0$. All the velocity profiles of interest here may have forward or reversed flow and moreover are continuous in y. Reversed flow in particular is mentioned briefly in passing, later, while Section 6 shows that nonlinear effects provoke profile discontinuities in effect.

3.1. For full profiles

For full profiles here the problem of solving (6a–c) or (6a,b,d,e) for $\tilde{\psi}$, and in particular finding c for given α, is a numerical one in general and usually c can be expected to be complex. This yields a standard, linear,

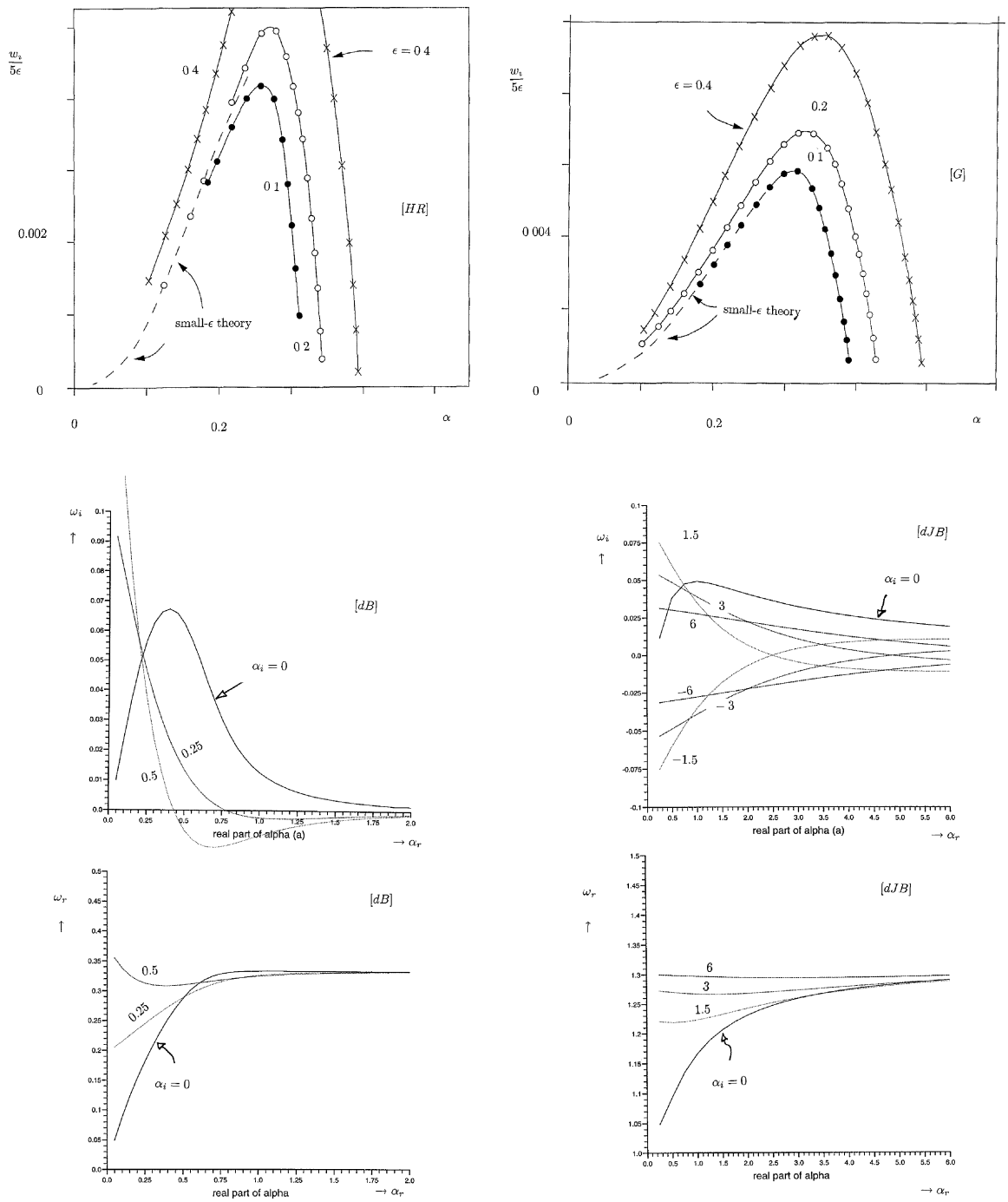

Figure 2. Solutions of the Rayleigh problem (6a–c or a,b,d,e). (a) For Hakkinen–Rott, Goldstein, double-Blasius and double-Jobe–Burggraf profiles. The additional factor ε in the first two cases here is explained in Section 3.1.

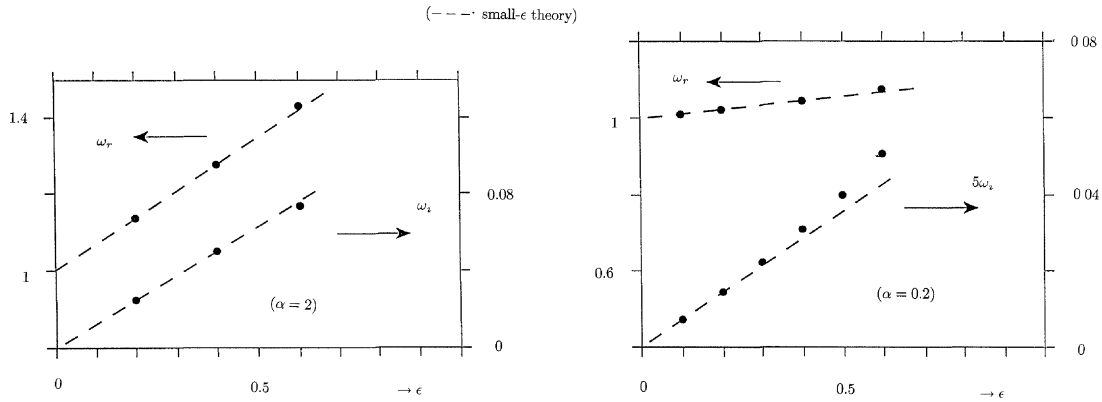

Figure 2. (Continued) (b) For profiles $\bar{u} = |y| + \varepsilon[1 - \exp(-|y|)]$, with various ε values. Both (a), (b) are also compared with small-ε theory.

computational investigation for complex α, c as in the Briggs–Bers techniques of earlier references; a more analytical investigation starts in Section 3.2, covering a wider variation of profiles. Numerical solutions for four main full profiles, Hakkinen–Rott, Goldstein, a representative double-sublayer profile and the double-Blasius case, are given in *figure 2*(*a*), the last two showing a range of unstable wavenumbers although no absolute instability is found yet; see also flow reversal later. The first two profiles are inflection-free and seem to be stable. Their corresponding results in *figure 2*(*a*) are for profiles $[\bar{u} - \varepsilon(y^2 + 1)^{1/2}]/(1 - \varepsilon)$, with relatively small positive values of ε and with $\bar{u}$ being the Hakkinen–Rott or Goldstein profile scaled such that λ is unity. Thus ε is added in order to highlight the absence of instability for those two profiles. The extra contributions in ε produce slight inflection at relatively large y values. The resulting instability tends to disappear as the additional factor ε is reduced towards zero, the instability then being confined to ever smaller $|\alpha|$ and larger $|y|$ values and illustrating a feature which is to be analysed in the following subsection. Again, the double-sublayer profile has $\bar{u} - |y| = \varepsilon(1 - \exp(-|y|))$ for $\varepsilon = 0.325$, which fits the calculated lower-deck profile of Jobe and Burggraf [28], at the trailing edge, to within about 2% for all y. Also presented are comparisons in *figure 2*(*b*), for varying ε values, with theoretical results for small ε obtained as in the next subsection. The comparisons indicate good agreement for ε between zero and about 0.5, say, including in particular the Jobe–Burggraf case above. Similar comparisons hold as shown in *figure 2*(*a*) for the Hakkinen–Rott and Goldstein cases at small $|\alpha|$ and the double-Blasius profile at large $|\alpha|$.

3.2. For near-uniform shears with or without influx

We suppose now that the profile $\bar{u}$ has the form of two nearly uniform shears, as remarked in Section 2, such that in effect

$$\bar{u} = \pm y + \varepsilon \bar{u}_1(y), \quad \text{for } y \gtrless 0, \tag{7}$$

with ε small and positive and $\bar{u}_1(y)$ typically of O(1) at O(1) values of y and continuous for all y (see also flow-reversal effects later, for example in equation (B16) in Appendix B). This is for (2); (3) is considered near the end of this subsection. The form (7) suggests seeking the solution for $\tilde{\psi}$ and c as expansions

$$\tilde{\psi} = \psi_0 + \varepsilon\psi_1 + \cdots, \qquad c = c_0 + \varepsilon c_1 + \cdots \tag{8a, b}$$

for fixed real α, where c_0, c_1, etc., may be complex. Substitution into (6a,b,d,e) therefore yields, in turn,

$$(\psi_0'' - \alpha^2\psi_0) = 0, \qquad (\pm y - c_0)(\psi_1'' - \alpha^2\psi_1) = \bar{u}_1''\psi_0, \tag{9a, b}$$

$$\psi_0(\pm\infty) = \psi_1(\pm\infty) = 0, \tag{9c, d}$$

$$\psi_0,\ \psi_1 \text{ are to be continuous across } y = 0, \tag{9e, f}$$

$$c_0\big(\psi_0^+\big)' + \psi_0^+ = c_0\big(\psi_0^-\big)' - \psi_0^- \quad \text{at } y = 0\pm, \tag{9g}$$

$$\big(c_0\psi_1^+ + \bar{c}_1\psi_0^+\big)' + \psi_1^+ + \lambda_1^+\psi_0^+ = \big(c_0\psi_1^- + \bar{c}_1\psi_0^-\big)' - \psi_1^- + \lambda_1^-\psi_0^- \quad \text{at } y = 0\pm, \tag{9h}$$

away from the critical levels $y = \pm c_0$. Here $\bar{c}_1 = c_1 - \bar{u}_1(0)$. The balance (9b) assumes that in (9a), while $\lambda_1^\pm$ in (9h) denote the interfacial shear values $\bar{u}_1'(0\pm)$.

The leading-order solution from (9a,c) has, with $A_0^\pm$ unknown constants,

$$\psi_0^\pm = A_0^\pm\tilde{e} \quad \text{with} \quad \tilde{e} \equiv \exp\big(\mp|\alpha|y\big), \tag{10a}$$

where (9e,g) require that

$$A_0^+ = A_0^-(\equiv A_0), \qquad -c_0A_0|\alpha| + A_0 = c_0A_0|\alpha| - A_0 \tag{10b, c}$$

respectively. Hence the dispersion relation at leading order is simply

$$(\omega_0 =)\alpha c_0 = \operatorname{sgn}(\alpha) \tag{11}$$

as in Papageorgiou and Smith [4], with $\omega(\equiv \alpha c) = \omega_0 + \varepsilon\omega_1 + \cdots$ denoting the frequency response; Dritschel [36] points out an equivalent result in a different setting. So at this level the flow solution reacts at a fixed frequency of $(\pm)1$ for any wavenumber α.

At the next level, the solution of the forced equation (9b) for ψ_1, given ψ_0 in (10a) and the constraints in (9d), yields

$$\psi_1^\pm = \left[\mp\tilde{e}\,\Xint=_0^y \frac{\bar{u}_1''(\tilde{y})\,\mathrm{d}\tilde{y}}{(\pm\tilde{y} - c_0)} \pm \tilde{e}^{-1}\,\Xint=_{\pm\infty}^y \frac{\bar{u}_1''(\tilde{y})e^{\mp2\gamma\tilde{y}}\,\mathrm{d}\tilde{y}}{(\pm\tilde{y} - c_0)}\right]\frac{A_0}{2\gamma} + A_1^\pm\tilde{e} \tag{12}$$

with unknown constants $A_1^\pm$ and with $\gamma = |\alpha|$. The double bar in the integrals signifies inclusion of jumps across $\tilde{y} = \pm c_0$ as well as principal values. Then (9f,h) in turn impose the balances

$$[K_1 \equiv]A_1^+ + A_0(2\gamma)^{-1}I_1 = A_1^- - A_0(2\gamma)^{-1}I_2, \tag{13a}$$

$$c_0\big\{I_1A_0/2 - \gamma A_1^+\big\} - \bar{c}_1\gamma A_0 + K_1 + \lambda_1^+A_0 = c_0\big\{I_2A_0/2 + \gamma A_1^-\big\} + \bar{c}_1\gamma A_0 - K_1 + \lambda_1^-A_0, \tag{13b}$$

from which the dispersion-relation correction

$$(\omega_1 =)\alpha c_1 = \frac{1}{2}\big[c_0(I_1 - I_2) + \big(\lambda_1^+ - \lambda_1^-\big)\big]\operatorname{sgn}(\alpha) + \alpha\bar{u}_1(0) \tag{14a}$$

is obtained on use of (11), where the integrals

$$I_1 \equiv \Xint=_\infty^0 \frac{\bar{u}_1''(\tilde{y})e^{-2\gamma\tilde{y}}\,\mathrm{d}\tilde{y}}{(\tilde{y} - c_0)}, \qquad I_2 \equiv \Xint=_{-\infty}^0 \frac{\bar{u}_1''(\tilde{y})e^{2\gamma\tilde{y}}\,\mathrm{d}\tilde{y}}{(-\tilde{y} - c_0)} \tag{14b, c}$$

are complex in general. Since c_0 is real the disturbance growth rate stems predominantly from c_{1i} and hence from the imaginary part of $(I_1 - I_2)$. The latter part is given by the jumps in phase across the two critical levels $y = \pm c_0 = \pm\gamma^{-1}$, these jumps corresponding to local replacement of $\ell n|y \mp c_0|$ as $y \to \pm c_0$ from below in (14b,c) by $\ell n(y \mp c_0) + i\pi$ sgn $(\alpha\bar{u}')$ from above, provided that the embedded critical layers (viscous and/or unsteady) remain linear; see references in Section 1, and compare with later sections on nonlinearity. It follows that the dominant growth rate is given by

$$\omega_i = \varepsilon\alpha c_{1i}, \quad \text{with} \quad \alpha c_{1i} = \frac{-\pi\{\bar{u}_1''(c_0) + \bar{u}_1''(-c_0)\}}{2e^2\gamma}, \tag{15}$$

a result which agrees with Papageorgiou and Smith's [4] (3.8) for their special case. The same results are obtained by an alternative approach of subdividing the total flow region into four subregions, above and below the critical levels for each of $y > 0$, $y < 0$, and then dealing with real integrals and their finite parts rather than (12)–(14b,c), as in Section 5 below. The predictions (14a)–(15) for small ε are used in the comparisons in *figure 2*(*a*),(*b*). Some further points and examples are presented in Appendix A.

Similar analysis applies for (3). Here (9b,h) are altered by setting $\lambda_1^{\pm} = \bar{u}_1'' = 0$ but adding $\pm B(\psi_0^{\pm})''/(i\alpha)$ to the left and right sides respectively of (9h). Compare (6e). The remainder of the working is similar, leading to the result $\bar{c}_1 = -i\gamma B/\alpha$ and hence

$$\omega_i = -\varepsilon\gamma B. \tag{15′}$$

As the influx B is positive, the effect in (15′) is stabilising and (15) it follows that for the cases (2) there are two time scales, of orders 1 (stage I) and ε^{-1} (stage II), for the linear disturbance, in the first of which a fixed-frequency response holds with algebraic amplitude growth at most, as εt is small, while in the second exponential amplitude growth or decay may emerge. Cases (3) exhibit the same feature. These two time scales form the basis for the remainder of the paper especially concerning nonlinear features, after the examination of the linear large-time behaviour in the next subsection.

3.3. Examples, and large-time instability

Here the flows of (2) are addressed, as the response for the flows (3) is already clear from (15′). The case of a distortion profile $\bar{u}_1$ symmetric in y and a general initial condition symmetric in x about $x = x_1$ say seems representative, leading to the typical disturbance solution

$$\pi\hat{q}(x,t) = \mathcal{J}_1\cos t + \mathcal{J}_2\sin t, \tag{16a}$$

$$\mathcal{J}_1 + i\mathcal{J}_2 = \int_0^{\infty} \hat{q}^*(\alpha)\exp\big[i\alpha x + \big(g_1(\alpha) + ig_2(\alpha)\big)T\big]\,\mathrm{d}\alpha \tag{16b}$$

from (14a–c), (15) with (11), interpreted in terms of a Fourier transform in $x(\to\alpha)$. In (16b), $\hat{q}^*$ is the initial transform, $t = \varepsilon^{-1}T$ defines the slow time of stage II, and

$$g_1 = -\frac{\bar{u}_1''(\alpha^{-1})\pi\chi}{e^2\alpha}, \qquad g_2 = \fint_0^{\infty} \bar{u}_1''(y)\frac{e^{-2\alpha y}\,\mathrm{d}y}{(\alpha y - 1)} - \alpha\bar{u}_1(0), \tag{16c, d}$$

the effective slow complex frequency Ω being $-g_2 + ig_1$. We note that the local nature of the formula for g_1 above and the global form for g_2 are in keeping with comments in Woodley and Peake [5] on their computed behaviour of complex frequencies. The above has χ unity for real α, whereas if α becomes complex χ is

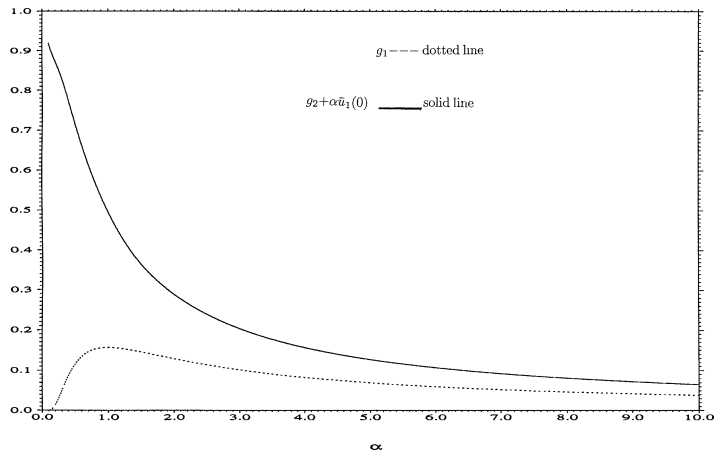

Figure 3. Plot of $g_1(\alpha)$, $g_2(\alpha)+\alpha\bar{u}_1(0)$ for distortion curvature $\bar{u}_1'' = -\exp(-y)$, in symmetric cases; see also Appendix B.

zero or two depending on whether α_i is negative or positive respectively. The single bar in the integral sign denotes the Cauchy principal value in the real case. Here we may absorb the centre-line shears $\lambda_1^{\pm}$ simply into an extra constant frequency response as seen in $(\lambda_1^+ - \lambda_1^-)$ in (14a), additional to the main frequency response in (11), and x_1 is taken as zero, for the sake of clarity. In addition the same results (16a–d) apply for a nonsymmetric profile provided that $\bar{u}_1(y)$ in (16c,d) is replaced by the average profile $[\bar{u}_1(y)+\bar{u}_1(-y)]/2$ (see also *figure 1*(*d*)–(*f*)), and likewise for $\bar{u}_1''(\alpha^{-1})$, $\bar{u}_1'(0)$, because of the general results (14a–c), (15).

The precise behaviour at large times T depends on the specific distortion profile $\bar{u}_1(y)$; many examples are mentioned in Sections 1, 2, while *figure 2*(*a*) indicates also the numerical validity of using a distortion profile. Three features are clear here, however. First, as a general rule unstable growth in the current near-wake is associated with $\bar{u}_1''$ being negative, and therefore more with a favourable streamwise basic pressure gradient (at least on the fixed surface upstream) than with an adverse one, in contrast with totally wall-bounded configurations; the aligned flat plate for example has such a favourable pressure gradient upstream and so exhibits the present near-wake instability (again see *figure 2*(*a*)). This change in stability characteristics as the flow leaves a trailing edge is in line with the curvature reversal which is implicit inside/near the thin Hakkinen–Rott or Goldstein viscous layer close to the centre-line. Second, increasingly negative values of $y\bar{u}_1''$ can play a substantial role in the growth as the following properties show. The third feature here is that absolute instability is a distinct possibility, based on Briggs–Bers reasoning coupled with the present analytical approach. Moreover, the addition of (even slight) flow reversal, decreasing $\bar{u}$ by a positive amount $\bar{u}_r$, is equivalent here to decreasing ω by $\alpha\bar{u}_r$ as demonstrated in (14a) which can readily produce absolute instability; conversely, slight additional forward motion can readily change absolute instability to downstream convective instability, again via (14a). The examples in Appendix B (and see *figure 3*) demonstrate these points for symmetric and nonsymmetric profiles, with the maximal α being real or complex depending on the $\bar{u}_1(y)$ profile.

The following sections address the two temporal stages I, II in more structural detail, partly to clarify the linear behaviour itself in each stage, supplementing what has been shown in this section, but more especially to incorporate significant nonlinear features, for initial-value settings.

4. Temporal stage I: linear and nonlinear effect

A check must be made on transients during this first temporal stage. The working is couched now in terms of the nonlinear unsteady Euler flow problem

$$\underline{u} = (\psi_y, -\psi_x), \tag{17a}$$

$$\underline{u}_t + (\underline{u}.\underline{\nabla})\underline{u} = -\underline{\nabla} p, \tag{17b, c}$$

for $\underline{u} = (u, v)$ and p as functions of x, y, t, with $\underline{\nabla}$ denoting (∂_x, ∂_y),

$$v = f_t + uf_x, \quad p \text{ continuous, across } y = f(x,t), \tag{17d}$$

where the interface shape $f(x,t)$ is unknown, and

$$\underline{u} \sim \big(|y| + \varepsilon \bar{u}_1(y), \mp \varepsilon B\big) \quad \text{as } x^2 + y^2 \to \infty. \tag{17e}$$

Again the parameter ε is small, and the distortion profile $\bar{u}_1$ is assumed to be smooth in y and suitably bounded at large $|y|$, for the cases (2) of zero B considered now; (3) is similar.

With an amplitude factor Δ representing the disturbance size, the expansion

$$[u, v, p, f] = [\pm y + \varepsilon \bar{u}_1, 0, 0, 0] + \Delta[u_0 + \varepsilon u_1, v_0 + \varepsilon v_1,\ p_0 + \varepsilon p_1, f_0 + \varepsilon f_1] + \cdots \tag{18}$$

is expected to hold here. The factor Δ will be decided upon subsequently but for now we take Δ to be much smaller than any power of ε. Substitution into (17a–e) then yields the successive controlling equations as follows.

4.1. Linear behaviour

At leading order $(\partial/\partial t \pm y\partial/\partial x)(\nabla^2 v_0)$ is zero from (17a–c) and so a possible form has

$$\nabla^2 v_0 = \nabla^2 u_0 = 0, \qquad \nabla^2 p_0 = \mp 2 v_{0x}, \tag{19a}$$

cf. Stewartson [45,46]. Then (17d) requires

$$v_0| = f_{0t}, \qquad (\pm v_{0x} - v_{0yt})| \text{ to be continuous}, \tag{19b, c}$$

where the vertical line denotes evaluation at $y = 0\pm$. The solution of (19a) for the Fourier transform in x $(\to \alpha)$ gives $v_0^* = f_{0t}^* \exp(\mp\gamma y)$, with (19c) demanding that $i\alpha f_{0t}^* + \gamma f_{0tt}^*$ be zero, so that

$$f_{0t}^* = d_0^*(\alpha) e^{-i\alpha t/\gamma} \tag{20}$$

with the initial transform function $d_0^*(\alpha)$ arbitrary, and hence $f_0^* = \gamma d_0^*(1 - \exp(-i\alpha t/\gamma))/(i\alpha)$ if the shape f_0 is zero initially. The response (20) is in line with the constant-frequency result (11). In real space, which is more suitable for the ensuing nonlinear study, the solution has

$$v_{0x} = \frac{y}{\pi} \int_{-\infty}^{\infty} \frac{G(s,t)\,\mathrm{d}s}{(x-s)^2 + y^2} \tag{21a}$$

with

$$G(\equiv D_x) = G_1 \cos t + G_2 \sin t, \tag{21b}$$

where $D(x,t) \equiv f_{0t}$ and the initial value is $D(x,0) = d_0(x)$. Here the real functions G_1, G_2 are inter-related by

$$G_1(x) = -\mathcal{L}(G_2), \qquad G_2(x) = \mathcal{L}(G_1), \tag{21c, d}$$

$$\mathcal{L}(G(x)) \equiv \frac{1}{\pi} \int\!\!\!\!\!\!- _{-\infty}^{\infty} \frac{G(s)\,\mathrm{d}s}{(x-s)}, \tag{21e}$$

each of (21c,d) implying the other, so that $G_2(x)$ (say) is left arbitrary, determined by the particular initial condition. Further, the transforms corresponding to (21c,d) each give $\gamma G_1^* = i\alpha G_2^*$, again in keeping with (11) as well as (20). In this section we are concerned mainly with general non-wave initial conditions, for example such that $G_2(x)$ has compact support (a Gaussian input, say); wave-like input will be reconsidered near the end of this section however and then in the subsequent one.

The next-order balances produce the governing equation

$$(\partial_t \pm y\partial_x)\nabla^2 v_1 = \bar{u}_1''(y)\frac{\partial v_0}{\partial x} \tag{22}$$

for v_1, provided that Δ is sufficiently small. Consequently, if $\nabla^2 v_1$ is zero initially, then for positive times t

$$\nabla^2 v_1 = \frac{\bar{u}_1''}{2\pi} \int_{-\infty}^{\infty} \frac{e^{i\alpha x - \gamma y}}{(1-\gamma y)} \left\{ \left(\frac{i\alpha}{\gamma}\right) \sin t - \cos t + e^{-i\alpha y t} \right\} G_2^*(\alpha)\,\mathrm{d}\alpha, \tag{23}$$

indicating creation of non-uniform vorticity; (23) is shown for positive y, there being a similar result for negative y, and we have in mind principally the case of a symmetric $\bar{u}_1(y)$ distortion profile again. The result (23) can be re-written as

$$\nabla^2 v_1 = \frac{\bar{u}_1''}{2\pi} \left[e^{it} \hat{A}(x,y,t) + \mathrm{CC} \right], \tag{24a}$$

where

$$\hat{A}_t = i \int_0^{\infty} e^{i\alpha x - \alpha y} e^{it(1-\alpha y)} G_2^*(\alpha)\,\mathrm{d}\alpha \tag{24b}$$

and $\hat{A}(x,y,t)$ is zero at time $t = 0$. The behaviour implied by (24a) especially at large t is key in what follows.

4.2. Large times, and examples

A specific non-wave case is examined first, namely the algebraically decaying Witch-of-Agnesi input

$$G_2 = \frac{\pi^{-1}\sigma}{(\sigma^2 + x^2)}, \quad \text{so that} \quad G_2^* = e^{-\sigma\gamma}. \tag{25a}$$

Here the constant σ is positive, and (25a) yields a delta function in the limit as σ tends to zero. Now (24b) gives

$$\hat{A}(x,y,t) = i \int_0^t \frac{e^{i\tilde{t}}\,\mathrm{d}\tilde{t}}{y + \sigma + i(y\tilde{t} - x)} \left[\equiv iy^{-1}K \right]. \tag{25b}$$

Thus $\hat{A}$ is O(1) in general as $t \to \infty$, in the bulk of the flow. Also, strictly we cannot take the Fourier transform of $\hat{A}(x,y,\infty)$ as $\hat{A}$ is found to radiate, downstream, a wave of streamwise extent $|x| = \mathrm{O}(yt)$: see later. From

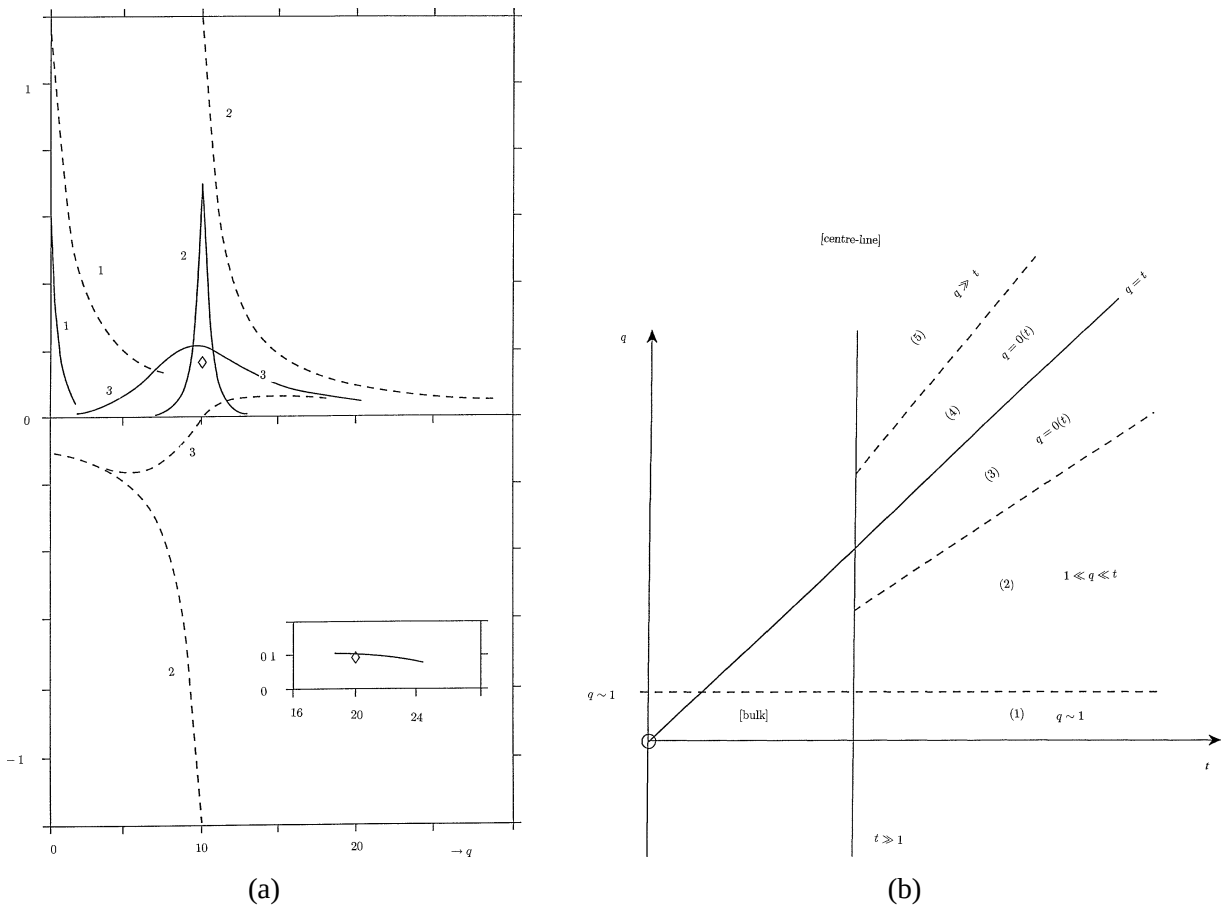

(a) (b)

Figure 4. (a) Real part (solid) and imaginary part (dashed) of $L_c(-q)$ and $L_c(t-q)$, in (26a,b), for zero σ, denoted 1, 2 respectively, and of $L_c(-q)$ for $\sigma = 0.5$, denoted 3, at $t = 10$. Note that the dashed curve 2 is finite at $q = 10\pm$, with solution values $\pm\pi/e$ $(= \pm 1.1557)$ respectively, while the solid curve 2 has the value 0.6972. The inset is at $t = 20$, for $\sigma = 0.5$. The diamonds indicate limit values as $t \to \infty$ for $\sigma = 0.5$. (b) Properties in the q–t plane, where $q \equiv x/y$; in regions 1–5, K is given by $K_1 + iL_d + \mathrm{O}(t^{-1})$, K_1, $K_1 - iL_c \exp(it) + \mathrm{O}(q^{-1})$, $-iL_c \exp(it) + \mathrm{O}(q^{-1})$, $\mathrm{O}(q^{-1})$, respectively, where K_1 denotes $2\pi \exp(iq - \Gamma)$ and L_d is the value of L_c at $t = 0$.

contour integration the vorticity-related function K can be expressed in terms of $q(\equiv xy^{-1}), t$ as

$$K = \pi_1 - ie^{it} L_c(t-q) + iL_c(-q), \tag{26a}$$

where π_1 is $2\pi \exp(iq - \Gamma)$ for $t > q$ but zero for $t < q$, $\Gamma \equiv 1 + \sigma y^{-1}$, and

$$L_c(t-q) \equiv \int_0^\infty \left[\Gamma - r + i(t-q)\right]^{-1} e^{-r}\, \mathrm{d}r. \tag{26b}$$

Here $L_c \sim (\Gamma + i(t-q))^{-1} \to 0$ as $(t-q) \to \pm\infty$ with $|q| \leqslant \mathrm{O}(t)$. Again, as $y \to 0+$ at finite positive x, t (26a) indicates that K tends to zero in proportion, leaving $\hat{A}$ as O(1) there. Representative computations for the real and imaginary parts of L_c (which helps to control the evolution of vorticity by means of (24a), (25b), (26a)) and a summarizing sketch are presented in *figure 4*(*a*), (*b*) given the importance of the large-time asymptotes in the subsequent nonlinear theory, *figure 4*(*a*) also contains comparisons with the large-time

predictions, indicating good agreement, while *figure 4*(*b*) indicates the large-time response of the vorticity function K.

The general non-wave case, second, follows from setting σ to zero and Γ to unity in the above, to accommodate a delta-function input, and then using convolution with the general $G_2(x)$ distribution as implied in (24b). The implications for the general case are analogous with those for nonzero σ above.

To see more clearly the presence of amplitude growth due to $\bar{u}_1$ as time increases we return to the boundary conditions (17d,e), with (24a), and derive the interfacial shape correction equation

$$f_{1xt} + \mathcal{L}(f_{1ttx}) = \kappa_1 e^{-it} + \mathrm{CC}\left[\equiv -\frac{\partial_t}{\pi} \int_0^\infty \left(\int_{-\infty}^\infty \left\{ \frac{y r_1(x-s,y)}{s^2+y^2} \right\} \mathrm{d}s \right) \mathrm{d}y \right] \tag{27}$$

at large t, where $r_1(x, y)$ is the right side of (13a) then. Therefore the shape correction is given by

$$f_{1xt} = (\hat{g}_1 t + \hat{h}_1)\cos t + (\hat{g}_2 t + \hat{h}_2)\sin t \tag{28a}$$

with

$$\hat{g}_2 = \kappa_{1r} - \mathcal{L}(\kappa_{1i}), \qquad \hat{g}_1 = \kappa_{2i} - \mathcal{L}(\kappa_{2r}), \qquad \kappa_2 = \kappa_1^{\mathrm{CC}}, \tag{28b}$$

determining the main temporal growth terms. Here for the delta-function input, for instance,

$$\kappa_1 = -\frac{1}{2\pi i} \int_0^\infty \bar{u}_1''(y)\hat{B}(x,y)\,\mathrm{d}y \tag{28c}$$

with $\hat{B}(x, y)$ equalling $\hat{A}(x, y, \infty)$ but with σ replaced by y and hence $\hat{B}$ is $iy^{-1}(\pi_1 + iL_c(-q))$ with Γ replaced by 2. Thus there is in effect a radiative part (π_1), which is an eigensolution wave persisting as $q(= x/y) \to \infty$ and corresponding to a downstream travelling zone of extent $(x - yt) \sim 1$, and a confined part $(L_c(-q))$ which decays as q^{-1} as $q \to +\infty$. Both of these parts in fact contribute to the amplitude growth represented by $\hat{g}_1, \hat{g}_2$, via the linear growth of f_1 inferred from (28a) (cf. (20)) which yields at large t a temporal growth rate f_{1xt}/f_{0x} coinciding with that of (15) when integrated over all α values; see also Appendix A.

4.3. Nonlinear effects

Finally here nonlinear influences are considered, associated with increasing the amplitude factor Δ in (18). The distinction between (i) input waves and (ii) input general (non-wave) disturbances at time $t = 0$ then becomes more significant. The initial input (i) of a wave or a superposition of waves is still covered by much of the preceding working as in effect each wave with streamwise wavenumber α_0 yields $G_2^*(\alpha)/(2\pi)$ proportional to a delta function $\delta(\alpha - \alpha_0)$. Thus (23) becomes for each distinct α

$$\nabla^2 v_1 = \bar{u}_1'' e^{i\alpha x - \gamma y} \gamma \hat{d}_0 \left[\frac{e^{-i\alpha t/\gamma} - e^{-i\alpha y t}}{\gamma y - 1} \right] + \mathrm{CC}, \tag{29}$$

satisfying (22), with initial condition $d_0(x) = \hat{d}_0 \exp(i\alpha x) + \mathrm{CC}$ where $\hat{d}_0$ is a constant. The flow solution is smooth for all finite t, even at the critical level $\gamma y = 1$ since the numerator in square brackets in (29) vanishes there. At large t however a critical layer starts to emerge. Letting $t \to \infty$ with fixed y in the core motion, away from the critical level and from the interface, tends to accentuate the $\exp(-i\alpha t/\gamma)$ term in (29), i.e. $\exp(\pm it)$, in agreement with (9b), (10a), (11), whereas in the emerging critical layer where $y = \gamma^{-1} + \mathrm{O}(t^{-1})$ the variation

of the $\exp(-i\alpha yt)$ term becomes O(1). The latter term smooths out the singular $(\gamma y-1)^{-1}$ behaviour from the former (core) term through the critical layer, and on integration it induces the $i\pi$ jump mentioned previously, but otherwise its fast-varying contribution to v_1 is comparatively small. Hence that core singularity has the form $v_1 \sim b_0 + b_{1L} s\ell n|s| + \mathrm{O}(s)$ as $s \equiv (y-\gamma^{-1}) \to 0\pm$, where $b_0(x,t)$ depends on the overall integration of $\nabla^2 v_1$, as in (12), (27), while $b_{1L} = \bar{u}_{1c}'' \hat{d}_0 \exp(i\alpha x - i\alpha t\gamma - 1) + \mathrm{CC}$ from (29), with the subscript c denoting evaluation at the critical level $y = \gamma^{-1}$. Considering increased Δ, therefore, the $\mathrm{O}(t^{-1})$ critical layer necessary in this case (i) has the inertial operator $(\partial/\partial t + y\partial/\partial x)$ typically becoming $\mathrm{O}(t^{-1})$ whereas the operator $v\partial/\partial y$ becomes $\mathrm{O}(t\Delta)$ from (18), when t is large. So the critical layer will feel the onset of a nonlinear influence when $\Delta \sim t^{-2}$, or at large times t of order $\Delta^{-1/2}$. This coincides with the second temporal stage II anticipated in Section 3 if $\Delta \sim \varepsilon^2$. The nonlinear development of case (i) for such amplitudes is followed through in the next section.

For general non-wave initial disturbances (ii), on the other hand, there are no corresponding singularities within the core, essentially because of the integration over α, as seen in (24a)–(26b). The smoothness of the core solution here even persists in the $\mathrm{O}(\varepsilon)$ neighbourhood of the interface (as $y \to 0+$, see near (26b)) despite the historical remains there associated with $x - yt$ remaining of O(1) when $x \sim 1,\ t \sim \varepsilon^{-1}$. The absence of critical layers for case (ii) means that the local nonlinear estimate above does not hold and instead global nonlinearity dominates, provoked by the interface reaction from (17d) in an amplitude-cubed manner, thus producing an $\mathrm{O}(\Delta^2)$ relative correction to the leading-order response (19a)–(21e). An analysis of this nonlinear effect, similar to that in Section 6 below and so omitted here, shows a growth term analogous with (28a) to be induced at large t. Comparison with the relative correction due to $\varepsilon\bar{u}_1$ in (22)–(28c) therefore indicates the crucial (lowest) amplitude scale $\Delta \sim \varepsilon^{1/2}$ for the subsequent nonlinear development in this general case (ii): see Section 6.

5. Temporal stage II: nonlinearity for pure wave input

Following on directly from item (i) just above, disturbance amplitudes Δ of $\mathrm{O}(\varepsilon^2)$ are of concern now, for an initial condition comprising a sum of pure waves, and here nonlinear critical layers are expected to arise as $t \to \varepsilon^{-1}T$ in stage II. Outside of these is the core flow $(\pm)$ for $y > 0,\ y < 0$, whose major properties of interest remain linear despite the jumps induced across each critical layer present. The core is examined in Subsection 5.1 below and the critical layers in Subsection 5.2, after which their solution features are described in Subsection 5.3. Again this cnsiders cases (2).

5.1. The core flow

The flow solution in the core has the expansion, implied by (18),

$$[u, v, p, f] = [\pm y + \varepsilon\bar{u}_1(y), 0, 0, 0] + \varepsilon^2[\tilde{u}_0, \tilde{v}_0, \tilde{p}_0, \tilde{f}_0] + \varepsilon^3[\tilde{u}_1, \tilde{v}_1, \tilde{p}_1, \tilde{f}_1] + \cdots . \tag{30}$$

For the moment we consider a single-wave input, with the $\mathrm{O}(\varepsilon^2)$ disturbances being proportional to $E^{\pm 1}$ and smooth in y, whereas in general the $\mathrm{O}(\varepsilon^3)$ contributions must contain all $E^{\pm n}$ terms for integer n, due to nonlinear critical-layer effects, and the $n = 1$ part is irregular at each critical layer because of the $\bar{u}_1$ distortion profile. The single-wave input (with wavenumber $\alpha > 0$) is written for convenience with $E = \exp(i\alpha x - it)$ where a scaled frequency of unity is still expected to apply from Sections 3 and 4, so that

$$\tilde{u}_0 = \tilde{\tilde{u}}_0\, E + \mathrm{CC}, \qquad \tilde{u}_1 = \sum_n \tilde{\tilde{u}}_{1n}\, E^n + \mathrm{CC} \tag{31}$$

and so on. Multiple waves will be discussed in Subsection 5.3. The expansions (30) are substituted into (17a–e) to provide the successive governing equations and boundary conditions.

The $O(\varepsilon^2)$ disturbances are therefore given by

$$[\,\tilde{\tilde{u}}_0, \tilde{\tilde{v}}_0, \tilde{\tilde{p}}_0\,] = [\,\mp i\,\tilde{\tilde{d}}_0, \tilde{\tilde{d}}_0, i\,\tilde{\tilde{d}}_0\,y]e^{\mp\alpha y}, \tag{32}$$

where, since $\tilde{v}_0 = \partial\tilde{f}_0/\partial t$ at $y = 0$ from (17d), $\tilde{\tilde{d}}_0 = -i\,\tilde{\tilde{f}}_0$ determines the interface perturbation in terms of the unknown amplitude $\tilde{\tilde{d}}_0\,(T)$. Thus $\tilde{v}_0$, $\tilde{p}_0$, $\partial\tilde{p}_0/\partial y$ are continuous across the centre-line $y = 0$ but $\tilde{u}_0$, $\partial^2\tilde{p}_0/\partial y^2$ are discontinuous there. The self-consistency at this level is in agreement with the fixed-frequency response anticipated in the form of E.

The $O(\varepsilon^3)$ perturbations, next, feel the influence both of $\bar{u}_1$ and of the critical-layer jumps. Addressing terms in E^n for $n \neq 1$ first, each $\tilde{\tilde{v}}_{1n} \propto \exp(\pm n\alpha y)$ from (17a–c) and is expected to be continuous at the upper critical level $y = \alpha^{-1}\ (= y_c) > 0$ but with a jump K_{1n}^+ (say) in $\partial\,\tilde{\tilde{v}}_{1n}\,/\partial y$ from y_c- to y_c+, while at the centre line $\tilde{\tilde{v}}_{1n}$ must equal $-ni\,\tilde{\tilde{f}}_n$ and $\tilde{\tilde{p}}_{1n}\,(\pm)$ must be continuous, from (17d). So the solution is

$$\tilde{\tilde{v}}_{1n}^{+} = d_{A,C}^{+}e^{-n\alpha y} + D_{A,C}^{+}e^{n\alpha y} \tag{33a}$$

in the regions A, C corresponding to $y > y_c$, $0 < y < y_c$ in turn, with analogous formulae holding for $y < 0$ including the lower critical layer. The required boundary conditions then give

$$D_A^+ = 0, \qquad \left(d_A^+ - d_C^+\right) = -\frac{K_{1n}^+e^n}{2\alpha n}, \qquad D_C^+ = -\frac{K_{1n}^+e^{-n}}{2\alpha n}, \tag{33b}$$

and similarly in the lower region, together with the coupling of the $\pm$ solutions across the interface as indicated above. That leaves the two relations

$$\begin{aligned}\left(d_A^- - d_A^+\right) &= \left(K_{1n}^+ + K_{1n}^-\right)\sinh(n)/(\alpha n),\\ \left(d_A^- + d_A^+\right) &= \left(K_{1n}^- - K_{1n}^+\right)\{\,\sinh(n) - n\,\cosh(n)\}/\left(\alpha n(1-n)\right),\end{aligned} \tag{33c, d}$$

which fix the functions $d_A^{\pm}$ in terms of the jumps across the critical level described later in Subsection 5.2. Thus the core contributions in E^n for $n \neq 1$ react passively. Moreover, since the values $K_{10}^{\pm}$ turn out to be zero the contributions for $n = 0$ are zero here.

The $n = 1$ forced contributions at $O(\varepsilon^3)$ in contrast are controlled by (9b) or (22) effectively and so

$$\tilde{\tilde{v}}_{11}^{\pm} = \frac{\tilde{\tilde{d}}_0}{2\alpha}\int_{\pm\infty}^{y}\frac{\bar{u}_1''(\tilde{y})}{(\tilde{y}\mp\alpha^{-1})}\left\{e^{\alpha(|y|-2|\tilde{y}|)} - e^{-\alpha|y|}\right\}\mathrm{d}\tilde{y} + \ell_A^{\pm}e^{-\alpha|y|} \tag{34a}$$

in regions A, while in regions C the lower limits of integration are taken as zero, ℓ_C replaces ℓ_A and terms $m_B^{\pm}\exp(\alpha|y|)$ are added to (34a). The critical-level constraints then require

$$Z_1^{\pm} \mp \alpha\left(\ell_A^{\pm}e^{-1} - \ell_C^{\pm}e^{-1} + m_C^{\pm}e\right) = K_{11}^{\pm}, \tag{34b}$$

$$Z_2^{\pm} + \ell_A^{\pm}e^{-1} = Z_3^{\pm} + \ell_C^{\pm}e^{-1} + m_C^{\pm}e, \tag{34c}$$

and the interface constraints impose the pressure balance

$$i\,\tilde{\tilde{d}}_{0T} = (m_C^+ + m_C^-) + \tilde{\tilde{d}}_0\,(\lambda_1^+ - \lambda_1^-)/2 + \tilde{\tilde{d}}_0\,\alpha\bar{u}_1(0) \tag{34d}$$

together with $(\ell_C + m_C)^{\pm}$ both being equal to $\partial\,\tilde{\tilde{f}}_0\,/\partial T - i\,\tilde{\tilde{f}}_{11}$. Here

$$Z_1^{\pm} = \mp\frac{\tilde{\tilde{d}}_0\,e}{2} - \int_0^{\pm\infty} \frac{\bar{u}_1''(y)}{(y \mp \alpha^{-1})}\left[e^{\mp 2\alpha y} + e^{-2}\right] \mathrm{d}y, \tag{35a}$$

$$2\alpha\left(Z_2^{\pm} - Z_3^{\pm}\right) = -\,\tilde{\tilde{d}}_0\,e\int_0^{\pm\infty} \frac{\bar{u}_1''(y)}{(y \mp \alpha^{-1})}\left[e^{-2\alpha y} - e^{-2}\right] \mathrm{d}y. \tag{35b}$$

Then (34b–d) yield the amplitude equation

$$\begin{aligned} i\,\tilde{\tilde{d}}_{0T} = {} & \frac{1}{2e\alpha}\left\{\left(Z_1^+ - Z_1^-\right) + \alpha\left(Z_2^+ - Z_3^+ + Z_2^- - Z_3^-\right) - K_{11}^+ + K_{11}^-\right\} \\ & + \tilde{\tilde{d}}_0\,(\lambda_1^+ - \lambda_1^-)/2 + \tilde{\tilde{d}}_0\,\alpha\bar{u}_1(0) \end{aligned} \tag{35c}$$

for $\tilde{\tilde{d}}_0\,(T)$, once the values $K_{11}^{\pm}$ are determined (as follows).

5.2. The nonlinear critical layers

For given positive wavenumber α the critical layer has $y \mp \alpha^{-1} = \varepsilon Y$ (upper and lower) and the expansion

$$\begin{aligned} [u, v, p] = {} & \Big[\alpha^{-1} + \varepsilon(\pm Y + \bar{u}_{1c}) + \varepsilon^2\left(\bar{u}_{1c}' Y + \tilde{u}_{0c}\right) + \varepsilon^3\left(\bar{u}_{1c}''\frac{Y^2}{2} + \hat{u}_1\right), \\ & \varepsilon^2\tilde{v}_{0c} + \varepsilon^3\left(\tilde{v}_{1c} + Y\tilde{v}_{0yc}\right) + \varepsilon^4\hat{v}_2, \\ & \varepsilon^2\tilde{p}_{0c} + \varepsilon^3\hat{p}_1 + \varepsilon^4\hat{p}_2\Big] + \cdots, \end{aligned} \tag{36}$$

with the subscript c denoting evaluation at $y = \pm\alpha^{-1}$ here. Additional terms in $\ell n\varepsilon$ play no role in the main amplitude evolution below. In consequence the controlling equation for each critical layer is found to be

$$\left\{\partial_T + (\pm Y + \bar{u}_{1c})\partial_x + \left(\tilde{\tilde{v}}_{0c}\,E + \mathrm{CC}\right)\partial_Y\right\}\hat{\tau}_1 = -\,\tilde{\tilde{v}}_{0c}\,\bar{u}_{1c}''E + \mathrm{CC} \tag{37a}$$

for the effective negative vorticity $\hat{\tau}_1 \equiv \partial\hat{u}_1/\partial Y - \partial(\tilde{v}_{0c})/\partial x$, subject to $\hat{\tau} \to 0$ as $|Y| \to \infty$ from matching with the solution in Subsection 5.1. Alternatively the equation can be expressed in terms of $\partial\hat{\tau}_1/\partial x = -\partial^2\hat{v}_2/\partial Y^2 - \partial^2(\tilde{v}_{0c})/\partial x^2$. In (37a), $\tilde{\tilde{v}}_{0c} = e^{-1}\,\tilde{\tilde{d}}_0$ from (32) and generally the dynamics is that of a nonlinear nonequilibrium critical layer.

The required jump contributions, which couple with (35c) to govern the disturbance amplitude $\tilde{\tilde{d}}_0\,(T)$, are therefore given by

$$K_{11}^{\pm} = \mp i\alpha(FP)\int_{-\infty}^{\infty}\hat{\hat{\tau}}_1\,\mathrm{d}Y. \tag{37b}$$

The double hat signifies the E component of $\hat{\tau}_1$, with other nonzero components $K_{1n}^{\pm}$ in E^n for $|n| \geqslant 2$ being generated by the presence of the nonlinear contribution in $\partial/\partial Y$ in (37a) as in Benney and Bergeron [48],

Haberman [49], Stewartson [50], Hickernell [51], Gajjar and Smith [52], Goldstein and Leib [53] and related papers. If the amplitudes present are relatively low then the combination of (37a,b) with (35c) reproduces the results of Section 3 as expected, agreeing with (14a–c), (15), (16c,d) with allowance for the $\bar{u}_1(0)$ factor here and below. For scaled amplitudes of order unity, on the other hand, the results of Section 3 apply only at small times T and we might expect an interesting new nonlinear interaction to emerge as time T increases, a point studied below.

5.3. Solution features

It is shown here that in fact the nonlinear interactions all seem to reduce to a problem studied previously, whether the input is a single wave or a superposition of waves.

The nonlinear single-wave interaction above can be normalised by using $Y \pm \bar{u}_{1c}$ in place of Y in each critical layer and setting

$$\begin{aligned}&\left[\hat{\tau}_1^{\pm},\ \tilde{\tilde{v}}_{0c},\ K_{11}^{\pm},\ x - t/\alpha,\ Y,\ T\right]\\ &\quad = \left[\sigma^{\pm}\tau^{\pm},\ \alpha e^{i\bar{\lambda}\bar{T}}\bar{V},\ -2ie^2\alpha^3 e^{i\bar{\lambda}\bar{T}}k^{\pm},\ \alpha^{-1}(\bar{\xi} - \lambda\bar{T}),\ \pm\bar{Y} \mp \bar{\lambda},\ \alpha^{-1}\bar{T}\right],\end{aligned} \tag{38}$$

where $\sigma^{\pm} \equiv (\bar{u}_{1c}'')^{\pm}$ and $\bar{\lambda}$ are real constants, $-\tilde{\tilde{d}}_0\,\alpha\bar{\lambda}$ equalling the right-hand side of (35c) minus the terms in $K_{11}^{\pm}$. That leaves the functions $\tau^{\pm}$, $\bar{V}$ controlled by

$$\left\{\partial_{\bar{T}} + \bar{Y}\partial_{\bar{\xi}} \pm (\bar{V}\hat{E} + \mathrm{CC})\partial_{\bar{Y}}\right\}\tau^{\pm} = -(\bar{V}\hat{E} + \mathrm{CC}), \tag{39a}$$

$$\frac{\mathrm{d}\bar{V}}{\mathrm{d}\bar{T}} = \frac{1}{2\pi}(FP)\int_{-\infty}^{\infty}\int_{0}^{2\pi}\left[\Gamma^{+}\tau^{+} + \Gamma^{-}\tau^{-}\right]\hat{E}^{-1}\,\mathrm{d}\bar{\xi}\,\mathrm{d}\bar{Y}, \tag{39b}$$

with the real parameters $\Gamma^{\pm} \equiv \sigma^{\pm}/(2e^2\alpha^2)$ and $\hat{E} \equiv \exp(i\bar{\xi})$, from (37a,b). The $\pm$ signs on the nonlinear term involving $\bar{V}\partial/\partial Y$ in (39a) are compatible with the evenness in y of the primary v disturbance in (32), and earlier, which is of sinusoidal form for each individual wave. The two upper and lower critical-layer problems here can be made identical from setting, in the lower one, $\bar{\xi} = \bar{\xi}_1 + \pi$, $\hat{E} = -\hat{E}_1 = -\exp(i\bar{\xi}_1)$ and $\tau^{-} = -\tau_1^{+}$, so that the lower critical-layer equation in (39a) is the same as the upper but with subscripts 1 inserted for $\bar{\xi}, \hat{E}, \tau^{+}$, and similarly for the Γ^{-} contribution in (39b) except that the range of integration in $\bar{\xi}_1$ is $(-\pi, \pi)$. Also, adding Γ^{+} times the upper critical-layer equation to Γ^{-} times the lower one now converts the nonlinear interaction to the form

$$\left\{\partial_{\bar{T}} + \bar{Y}\partial_{\bar{\xi}} + (\bar{V}\hat{E} + \mathrm{CC})\partial_{\bar{Y}}\right\}\tau = -\bar{\upsilon}(\bar{V}\hat{E} + \mathrm{CC}), \tag{40a}$$

$$\frac{\mathrm{d}\bar{V}}{\mathrm{d}\bar{T}} = \frac{1}{2\pi}(FP)\int_{-\infty}^{\infty}\int_{0}^{2\pi}\tau\,\hat{E}^{-1}d\bar{\xi}\,\mathrm{d}\bar{Y}, \tag{40b}$$

where $\bar{\upsilon}, \tau$ stand for $(\Gamma^{+} + \Gamma^{-})$, $(\Gamma^{+}\tau^{+} + \Gamma^{-}\tau_1^{+})$ respectively, together with decay conditions at large $|\bar{Y}|$. Consequently we are left with a nonlinear problem (40a,b), that is as if for a single critical layer. Solutions for this are described by Goldstein and Leib [53] (see also Goldstein and Hultgren [19]), essentially, although the latter work is in a context of spatial development for a forced disturbance, starting far upstream, rather than the present context of temporal-spatial development for a free disturbance from an initial state, the present starting condition being at time $\bar{T} = 0+$. Here, for small $\bar{T}$, the $(\bar{V}\hat{E} + \mathrm{CC})$ term in (40a) becomes negligible compared with the $\partial/\partial\bar{T}$ and $\bar{Y}\partial/\partial\bar{\xi}$ terms, both of which are $\mathrm{O}(\bar{T}^{-1})$, matching with the earlier temporal

stage I as described near the end of Section 4. That leaves the linear jump value $i\pi$ applying in effect with $k^{\pm} \sim \mp\pi \bar{V}\Gamma^{\pm}$ and $\mathrm{d}\bar{V}/\mathrm{d}\bar{T} \sim -\pi\bar{v}\bar{V}$ then, at small $\bar{T}$, consistent with the growth rate in (15) involving the average value $[(\bar{u}_{1c}'')^{+} + (\bar{u}_{1c}'')^{-}]/2$. At large times $\bar{T}$ in contrast we would expect the asymptotic behaviour addressed in Goldstein and Leib [53] and in Brown and Stewartson [54], Stewartson [50], Warn and Warn [55] and related papers, for large distances downstream in some cases, to hold here, yielding nonlinear vorticity roll-up accompanied by slow algebraic amplitude growth at most and probable nonlinear saturation.

The next question concerns what happens with a superposition of waves. That amounts to (31) and (32) containing, in $\tilde{v}_0$ say,

$$e^{-it}\sum_{m} \overset{\approx}{d}^{(m)}(T)\exp(im\alpha x \mp m\alpha y) + \mathrm{CC} \tag{41}$$

with frequencies ± 1 again and $\overset{\approx}{d}_0^{(1)} = \overset{\approx}{d}_0$ but, although positive, m is not necessarily an integer. The core response remains linear to the present order of working and so linear superposition applies there, with nonlinearity entering only through the critical layers, similarly to that in the previous subsection. Such nonlinearity however does not force interaction between any of the modes in (41), as each mode is regular except at its own distinct critical layer at $y = \pm(m\alpha)^{-1}$ and the nonlinearity above provokes only nth harmonics with frequencies $\pm n$ which do not give eigenfunctions, cf. the form (41). Again, in each distinct critical layer any other components induced nonlinearly, by the $v\,\partial u/\partial y$ inertial term effectively, and not proportional to $E^{\pm n}$ say as in Subsections 5.1, 5.2, have wavespeeds c different from α^{-1} and so are simply counterbalanced by a corresponding term $(\partial/\partial T + c\partial/\partial x)\tau_2$ involving a higher-order vorticity correction τ_2. Thus the linear superposition of the multiple waves persists even in the current nonlinear case at this level. Each wave acts separately, being governed by (40a,b) applied to its own wavenumber $m\alpha$.

The absence of mode interaction above, for input nonlinear waves, makes an interesting contrast with the more general case of non-wave nonlinear input below.

6. Temporal stage II: nonlinearity for non-wavelike initial conditions

The crucial disturbance size here for general non-wave input is $\Delta = \mathrm{O}(\varepsilon^{1/2})$, from item (ii) near the end of Section 4, leading to a nonlinear effect quite distinct from that of the previous section. This is for both (2) and (3) effectively. The argument below is presented first for negligible curvature distortion $\bar{u}_1''(y)$ and influx, in subsection 6.1, and then the additional influences of a nonzero $\bar{u}_1''(y)$ curvature profile and nonzero influx B are included in Subsection 6.2, followed by solution properties in Subsection 6.3. We note that in essence 6.1, 6.2 correspond to zero or nonzero $\bar{u}_1$ distortion velocity profiles respectively (as well as influx B) provided that the effects of $\bar{u}_1(0+)(=\bar{u}_1(0-)), \bar{u}_1'(0\pm)$ on the linear phase contribution are included.

6.1. For zero distortion $\bar{u}_1$ and zero influx B

With the amplitude factor $\Delta = \varepsilon^{1/2}$, then, the two time scales $t, \varepsilon t\ (=T)$ again govern the disturbance evolution, so that the temporal operator becomes $\partial/\partial t + \varepsilon\partial/\partial T$. The flow solution now expands in the form, implied by (18),

$$[u, v, p, f] = [\pm y, 0, 0, 0] + \varepsilon^{1/2}[u_1, v_1, p_1, f_1]^{\pm} + \varepsilon[u_2, v_2, p_2, f_2]^{\pm} + \varepsilon^{3/2}[u_3, v_3, p_3, f_3]^{\pm} + \cdots \tag{42}$$

for $y > 0,\ y < 0$ in turn, with similar expressions for the stream function ψ and velocity potential ϕ; see also Dritschel [36]. Slow dependence on time T is implicit in the working below, and all the quantities involved here are real.

At leading order, the disturbance velocities u_1, v_1 satisfy Laplace's equation in x, y, as do the higher-order velocity components also, from (17a–c), subject to boundedness at large distances and to centre-line conditions linearized from (17d). So the leading solution is similar to that in (20)–(21e), having

$$[v_1, u_1]^{\pm} = \pm\frac{1}{\pi}\int_{-\infty}^{\infty} \frac{[y,\ (x-\xi)]D(\xi,t,T)\,\mathrm{d}\xi}{(x-\xi)^2+y^2}\big\{ \equiv \pm\big[\mathcal{M}(D), \mathcal{N}(D)\big]\big\}, \tag{43a}$$

$$f_{1t} = D(x,t,T) \equiv D_1(x,T)\cos t + D_2(x,T)\sin t, \tag{43b}$$

where $D_1(x,0)$ represents the arbitrary but non-wave initial condition, D_1, D_2 are related by

$$D_1(x,T) = -\mathcal{L}(D_2), \qquad D_2(x,T) = \mathcal{L}(D_1) \tag{43c}$$

or in transforms $\gamma D_1^* = i\alpha D_2^*,\ \gamma D_2^* = -i\alpha D_1^*$, and the constant-frequency result, e.g. (11), again emerges as evident in (43b). The respective solutions for $\psi_1^{\pm},\ -\phi_1^{\pm}$ have D in (43a) replaced by Q, where $\partial Q/\partial x = -D$, which leaves u_1, ϕ_1 odd in y whereas v_1, ψ_1, p_1 are even, the pressure disturbance p_1 being given by $p_1 = -\partial\phi_1/\partial t \mp yu_1 \pm \psi_1$ for $y > 0,\ y < 0$ in turn and being continuous across $y = 0$, in keeping with (17d). Also $v_1^{\pm} = \partial f_1/\partial t$ at $y = 0\pm$ is continuous there. The initial conditions, which have $f_1 = F_1(x)$ say and u_1 nonzero at time zero [so $f_1 = F_1 + D_1\sin t + D_2(1-\cos t)$], are consistent with a match to the solution of Section 4 in the earlier temporal stage, while, to be strict, D_1 is an unknown function of $x, T, \ldots$ whose initial distribution $D_1(x,0,\ldots)$ is specified. Likewise

$$Q = Q_1(x,T)\cos t + Q_2(x,T)\sin \mathrm{t} \tag{43d}$$

with Q_1 or Q_2 specified as a function of x at time $T = 0+$. An evolution equation for Q_2 will be derived subsequently.

The second-order disturbed flow is driven by the centre-line requirements

$$\begin{aligned} &v_2 + f_1 v_{1y} = f_{2t} + (\pm f_1 + u_1) f_{1x} \quad &&\text{at } y = 0\pm, \\ &p_2^+ = p_2^- &&\text{at } y = 0\pm, \end{aligned} \tag{44a, b}$$

from (17d) and from the continuity of $\partial p_1/\partial y$ at the centre line. Substitution from (43a–d) therefore requires, at $y = 0\pm$,

$$v_2 = f_{2t} \pm D^{(2)}, \quad D^{(2)} \equiv D_1^{(2)}\cos 2t + D_2^{(2)}\sin 2t + D_3^{(2)}, \tag{44c}$$

where, with $\hat{G} \equiv (\frac{1}{2}F_1^2 + F_1 D_2)$,

$$D_1^{(2)} = \tfrac{1}{2}(D_1 D_1' - D_2 D_2'), \qquad D_2^{(2)} = \tfrac{1}{2}(D_1 D_2)', \qquad D_3^{(2)} = -D_1^{(2)} + \hat{G}' \tag{44d}$$

and the prime now denotes $\partial/\partial x$. Hence

$$[v_2, u_2]^{\pm} = \big[\mathcal{M}\big(D^{(2)}\big), \mathcal{N}\big(D^{(2)}\big)\big] \tag{45a}$$

are odd and even in y, respectively, while f_{2t} is identically zero, leaving $f_2 \equiv F_2(x)$ say, and p_2 is even in y, satisfying (44b), and is given by

$$p_2 = -\phi_{2t} \mp y u_2 \pm \psi_2 - \tfrac{1}{2}(u_1^2 + v_1^2). \tag{45b}$$

The solutions for ψ_2, $-\phi_2$ have $Q^{(2)}$ instead of $D^{(2)}$ in (45a), with $\partial Q^{(2)}/\partial x = -D^{(2)}$. The third-order disturbances are likewise forced by the centre-line conditions, such that at $y = 0\pm$

$$(p_3 + f_1 p_{2y} + f_2 p_{1y} + \tfrac{1}{2} f_1^2 p_{1yy}) \text{ must be continuous}, \tag{46a}$$

from (17d). The accompanying condition on v_3 is akin to that in (44a) and serves to fix f_{3t} but it does not influence the resulting main amplitude evolution below. Given that f_2 is $F_2(x)$, and $\partial p_2/\partial y$ may be evaluated from (45a,b) and $\partial p_1/\partial y$ (which is continuous), $\partial^2 p_1/\partial y^2$ from (43a–d), use of the centre-line formulae

$$p_3 = -\phi_{3t} - \phi_{1T} \pm \psi_3 - (u_1 u_2 + v_1 v_2) \quad \text{at } y = 0\pm \tag{46b}$$

leaves v_3 $(= \partial\phi_3/\partial y = -\partial\psi_3/\partial x)$ governed by Laplace's equation and the centre-line constraints

$$v_3 = D^{(3)}, \qquad (\phi_{3t} - \psi_3)^+ - (\phi_{3t} + \psi_3)^- = H \tag{47a}$$

at $y = 0$. Here our concern is with the forced $\sin t$, $\cos t$ components only, so that

$$H = h_1 \cos t + h_2 \sin t + \text{o.t.}, \quad h_1 \equiv 2Q_{2T} - J_1, \; h_2 \equiv -2Q_{1T} - J_2, \tag{47b}$$

where o.t. denotes other harmonic terms and

$$\begin{cases} J_1 \equiv -D_2\mathcal{L}(D_1^{(2)}) - D_1\mathcal{L}(D_2^{(2)}) + D_1'(D_2^2 - D_1^2) + D_2'(2D_1D_2) + 2D_2\mathcal{L}(\hat{G}') \\ \qquad +2D_1\hat{G}' + 4\hat{G}D_1', \\ J_2 \equiv 3D_1\mathcal{L}(D_1^{(2)}) + D_2\mathcal{L}(D_2^{(2)}) + D_2'(3D_2^2 - D_1^2) - 2D_1\mathcal{L}(\hat{G}') + 2D_2\hat{G}' + 4\hat{G}D_2', \end{cases} \tag{47c, d}$$

from (46a,b) with (45a,b),(43a–d), after some working. The influence of $F_2(x)$ cancels out above because of the continuity of $\partial p_1/\partial y$. Application of the Fourier transform in $x(\to \alpha)$ to (47a), as near (20), with $D^{(3)}$ written as a linear combination of $\cos t$, $\sin t$, therefore yields the solvability requirement $i\alpha h_1^* = |\alpha| h_2^*$ and hence, on inversion and appeal to (43c), the nonlinear amplitude equation

$$4\frac{\partial Q_2}{\partial T} = J_1 - \mathcal{L}(J_2) \tag{48}$$

for $Q_2(x, T)$ during the current stage II. In (48) J_1, J_2 are defined in terms of the unknown amplitude function Q_2 via (47c,d) along with (43c), (44d) and with the relations $\partial Q_n/\partial x = -D_n$ for $n = 1, 2$. The amplitude equation can be expressed alternatively in terms of Q_1 with Q_2, J_1, J_2 replaced in (48) by $Q_1, -J_2, J_1$ respectively. A study of (48) for small times T confirms the necessary match with the amplitude growth $(\propto T)$ of Q_2 emerging from the earlier stage I implied near the end of Section 4.

Solution properties for (48) are discussed in Subsection 6.3.

6.2. For nonzero $\bar{\mathbf{u}}_1$ *and/or* $\mathbf{B}$

The effect of a nonzero smooth distortion profile $\bar{u}_1(y)$ and/or influx B, for the same amplitude factor $\Delta = \varepsilon^{1/2}$ and a general non-wavelike initial condition, is simply to add the linear modulations of Subsection 3.2

to the nonlinear balance of (48), during stage II. The flow structure of the previous subsection otherwise stays intact in view of the findings in Section 4 on the large-t influence of $\bar{u}_1$ for smooth non-wave input as opposed to the wave-input case considered earlier; likewise for B.

Thus the amplitude equation now takes the form

$$4\frac{\partial Q_2}{\partial T} = \frac{2}{\pi}\int_{-\infty}^{\infty}(g_1 + ig_2)\,Q_2^*(\alpha, T)\exp[i\alpha x]\,\mathrm{d}\alpha + 4B\mathcal{L}(D_2) + J_1 - \mathcal{L}(J_2) \tag{49}$$

with $g_1(\alpha)$, $g_2(\alpha)$ being specified by (16c,d) for positive real α and being even in α apart from the final term in (16d). Here again the continuation with the earlier stage-I behaviour can be verified for small T by comparison of the extra linear terms in (49) with the linear contributions in (28a). The governing equation (49) reflects, on its right side, an interesting interplay between linear destabilisation (for negative $\bar{u}_1''$, as in Section 3.2), linear stabilisation from influx (B) and nonlinear modulation; if all of these are absent then the fixed-frequency response of (11) continues unaltered, as Q_2 and therefore Q_1 in (43d) are then independent of T.

6.3. Solution properties

Computational studies of (48), (49) were undertaken, based on spectral and compact-difference approaches. In the spectral scheme, Q_2 and its Cauchy integral are expressed as

$$\big[Q_2, \mathcal{L}(Q_2)\big] = \sum_{-\infty}^{\infty}\big[1, -i\ \mathrm{sgn}(k)\big]q_{2k}(t)e^{ikx}. \tag{50}$$

The nonlinear parts J_1, J_2 in (48) or (49) may thus be rewritten as sums of cubic products of the form $f_k q_{2k}(t)\exp(ikx)$, where the coefficient f_k involves k, k^2 or $\mathrm{sgn}(k)$. The linear parts are similarly written in terms of $q_{2k}(t)$. Using 100 modes provided sufficient resolution in general. The solution was marched forward in time using a fourth-order Runge–Kutta scheme, a timestep of 10^{-6} being required usually. In the compact-differencing scheme, an iteration procedure was performed to satisfy (49) at the current time level, each iteration applying standard compact differencing on a lagged version of (49). The initial condition on Q_1 was taken as $r_1\exp(-r_2x^2)$, with r_1, r_2 positive constants, while boundary conditions of zero Q_1, Q_1', etc., were imposed at suitably large $|x|$, accounting for the algebraic decay there (Appendix A). The Cauchy integrals were treated as in Li et al. [56]. The iterative solution at each time level was obtained from a 2×2 block system. After some trials, a transformation was employed to cluster grid points around the origin. Typically, the x-range covered is $(-10, 10)$ with a minimum step of 0.005, while the time step is 10^{-6}. The scheme is centred in x, although a backward-x scheme gave results which were less sensitive (to bursting, see below).

We describe the main results below, after commenting on short-scale secondary instability. A small perturbation $\propto \widetilde{D}_2\exp(ikx)$ in D_2, of high wavenumber k, responds neutrally ($\exp(-i\bar{\omega}t)$) at leading order but grows at higher order unless B is sufficiently large, such that

$$\bar{\omega}_r = -(D_2 + F_1)^2 k|k|, \tag{51a}$$

$$\left(\frac{\partial}{\partial T_1} + c_g\frac{\partial}{\partial x_1}\right)\widetilde{D}_2 = \big\{\big(D_2^2 + \tfrac{1}{2}F_1^2 + F_1D_2\big)_x + F_1D_{2x} - 4B\big\}|k|\widetilde{D}_2, \tag{51b}$$

from (49). Here the effective temporal and spatial operators are $(-i\bar{\omega}_r + \partial/\partial T_1)$, $(ik + \partial/\partial x_1)$ respectively, while $c_g = -2(D_2 + F_1)^2|k|$ is the group velocity of the perturbation and is negative, as is the phase velocity from (51a). This indicates upstream convection.

Starting with the computations for zero $\bar{u}_1$ and F_1 reveals three typical solution paths for the evolving amplitude $Q_2(x, T)$, determined by the size of the influx coefficient B and by the initial form of Q_2. There is a critical value of B above which the solution decays to zero for all x (*figure 5*(*a*)) and below which the solution exhibits a blow-up singularity, with given initial conditions. Thus for an initial state $q_{2k} \propto \exp(-k^2)$ (spectral approach), the amplitude apparently tends towards a travelling-wave form at first sight. This form may be found from (48) by assuming dependence on $x - ct$ and solving the resulting ordinary differential-integral equation; see *figure 5*(*b*). The wave travels upstream, with its speed c (< 0) depending on the amplitude. In the unsteady calculation however this travelling-wave form is found on closer inspection to be unstable as in (51b) and bursting is observed: *figure 5*(*c*). The initial state above is sufficiently small in amplitude at high wavenumbers that the short-scale growth is relatively damped at early times, being proportional to $(2D_2D_2' - 4B)|k|T$. In contrast the travelling wave itself has a large high-wavenumber component and so it is not surprising that higher modes are available to grow.

To compare further with (51a,b) we imposed an initial condition $q_{2k} \propto \exp(-|k|)$; again a nonlinear singularity (burst) is seen apparently to develop in the solution (*figure 5*(*d*)) within a finite scaled time. At a very early stage the short-scale growth is still damped by the initial condition. However as the singularity deepens and the second derivative Q_{2xx} becomes large in magnitude, the growth rate of the short waves increases, being proportional to $(2Q_{2x}Q_{2xx} - 4B)|kt|$ from (51b). Thus short-scale growth begins, as is shown in *figure 5*(*d*) (spectrally).

The form of this burst is

$$Q_{2xx} \sim (T_2 - T)^{-1/2}\bar{D}_2'(\eta), \quad \eta \equiv \frac{(x - x_s)}{(T_2 - T)^{\bar{\rho}}}, \tag{52}$$

as $T \to T_2-$ locally near $x = x_s$, with Q_2 ,D_2 remaining finite and the power $\bar{\rho} > 1/2$. The scales in (52) leave the right side of (49) intact nonlinearly (with $\bar{D}_2$, η, 0, 0, 0, 0 replacing D_2, x, g_1, g_2, B, F_1, etc. if $\bar{\rho} < 1$), whereas the left is replaced by $4\{\bar{\rho}\eta\bar{Q}_2' - (2\bar{\rho} - \frac{1}{2})\bar{Q}_2\}$. The solution can be obtained analytically if $\bar{\rho} - \frac{1}{2}$ is small. The computed spectral results give a $\bar{\rho}$ value of approximately 0.86. We also examined $(Q_{2xx})^{-2}$ versus t, numerically finding it to be nearly linear just prior to bursting. The developing spike in *figure 5*(*d*) initially moves slowly downstream but at around $t = 0.0006$ it reverses and travels upstream as it evolves further, cf. (51a,b). The influx term (B) is found numerically to be negligible in comparison with the nonlinear terms, at bursting, as expected from the above analysis with $\bar{\rho} = 0.86$.

The final example shown for zero $\bar{u}_1$,F_1 (*figure 5*(*e*)) has the initial condition $q_{2k} = \exp(-|k|^{3/4})$, to examine whether the growth rate $(2Q_{2x}Q_{2xx} - 4B)$ criterion also serves as a criterion for finite-time blowup. This choice has sufficiently large amplitude at high wavenumbers that the short-scale growth is not necessarily damped. By choosing B sufficiently large, we ensured that the above growth rate was initially negative for all x. On linear grounds, the solution is expected to exhibit short-scale growth only if this growth rate becomes positive for any x. As shown in *figure 5*(*e*), we found that the bursting occurred in some cases even when this linear growth rate was still clearly negative everywhere except very locally, due to nonlinear effects becoming significant then. Larger B always produces amplitude decay as in *figure 5*(*a*).

Another influence of initial conditions is through the interfacial term $F_1(x)$ in (47c,d). Its nonlinear effect, like that of B, exceeds the effect of typical $\bar{u}_1$ profiles in fact, because of the large $|k|$ behaviour in (51a,b). Including a representative $\bar{u}_1$ term was found to alter little the three distinct solution paths described above, although the development of the bursting was slightly accelerated. Strictly, the compact differencing scheme

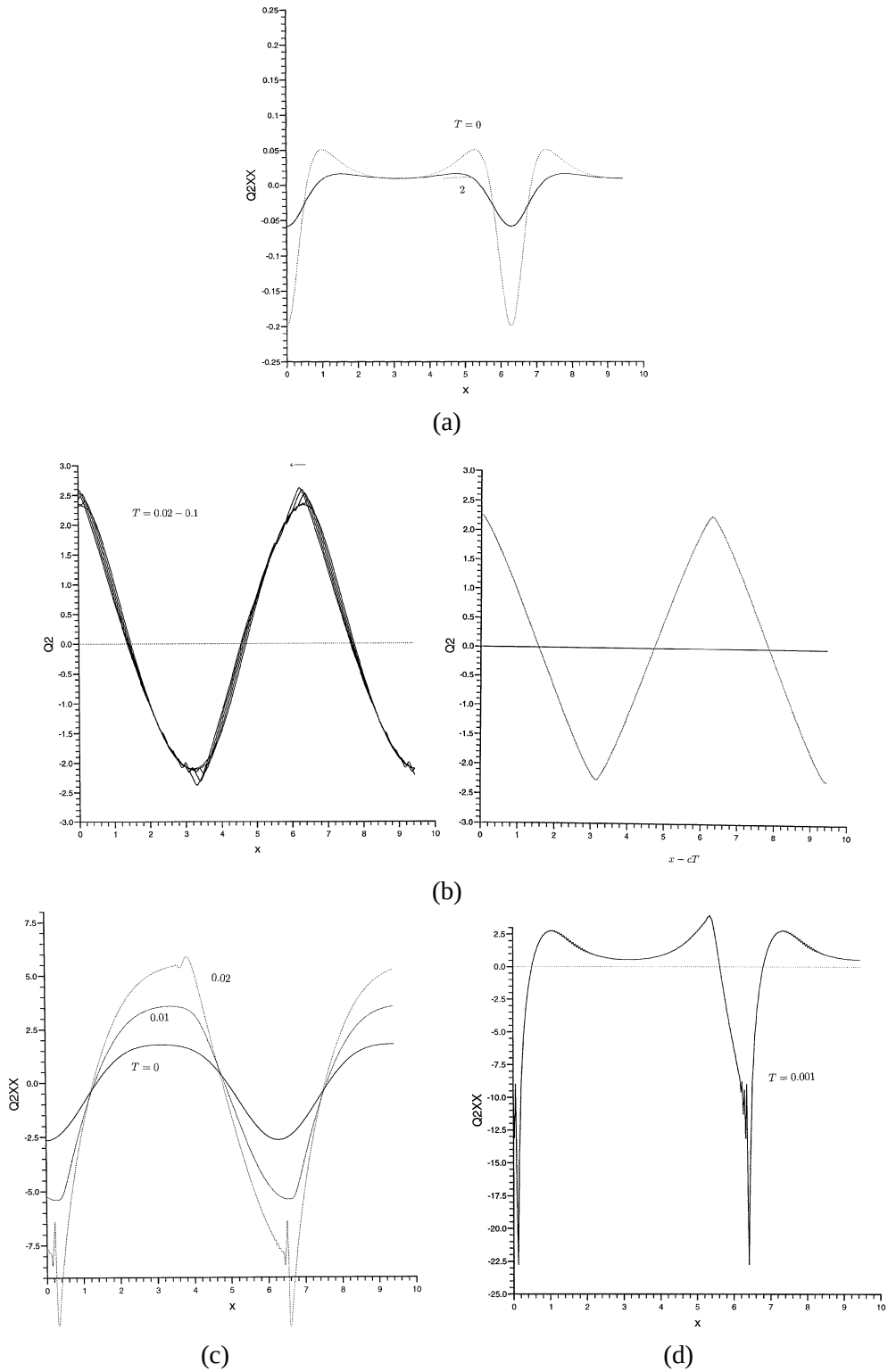

Figure 5. Computational solutions of (48) and (49) with zero $\bar{u}_1$, F_1 (spectral). (a) Initial condition $q_{2k} = 0.05\exp(-|k|)$, with $B = 0.25$. (b) Initial $q_{2k} = 3\exp(-k^2)$, $B = 0$; and comparison with travelling-wave solution. (c) As (b) but showing Q_{2xx}. (d) Initial $3\exp(-|k|)$, $B = 0$.

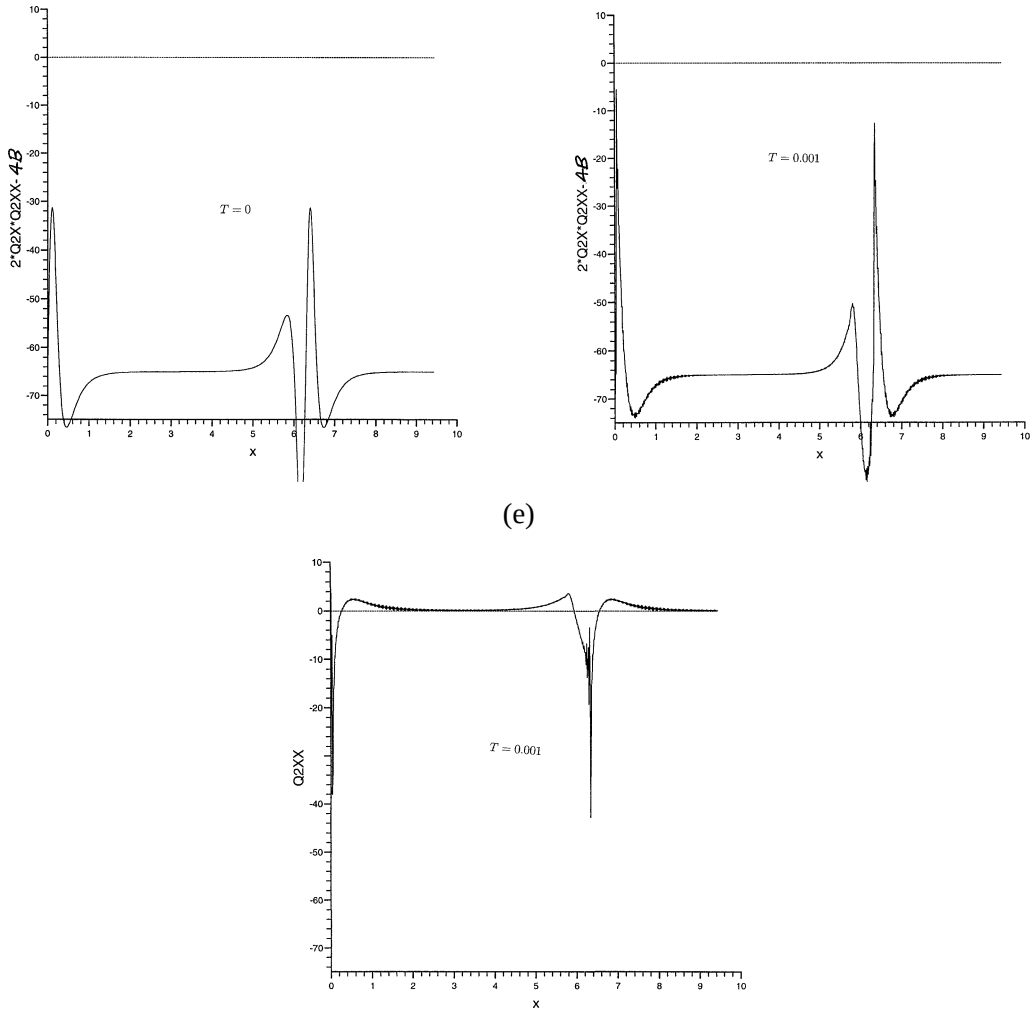

Figure 5. (Continued) (e) Initial $\exp(-|k|^{3/4})$, $B = 16.25$, showing $(2Q_{2x}\,Q_{2xx} - 4B)$ and Q_{2xx}.

should be used then, rather than spectral, in view of Section 5, but the results are similar and again stress the importance of the influx B (*figure 6*(*a*),(*b*)). The effect of a nonzero F_1 was more pronounced than $\bar{u}_1$, the computations showing a strong short-scale instability occurring sooner than in the previous case, at the onset of bursting or a travelling wave, in line with (51a,b). A sufficient increase in B damps out the effect (*figure 6*(*b*)).

7. Further comments

7.1. Direct implications

This investigation has focussed on the influences from concentrated layers with nonuniform vorticity, from sublayer influx and from nonlinear dynamics on the evolution of a disturbance in a near-wake, along with

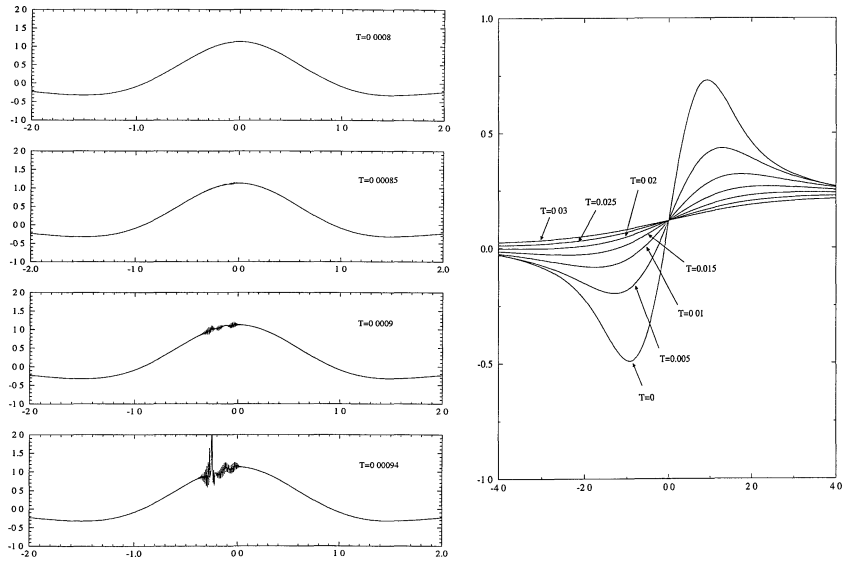

(a)

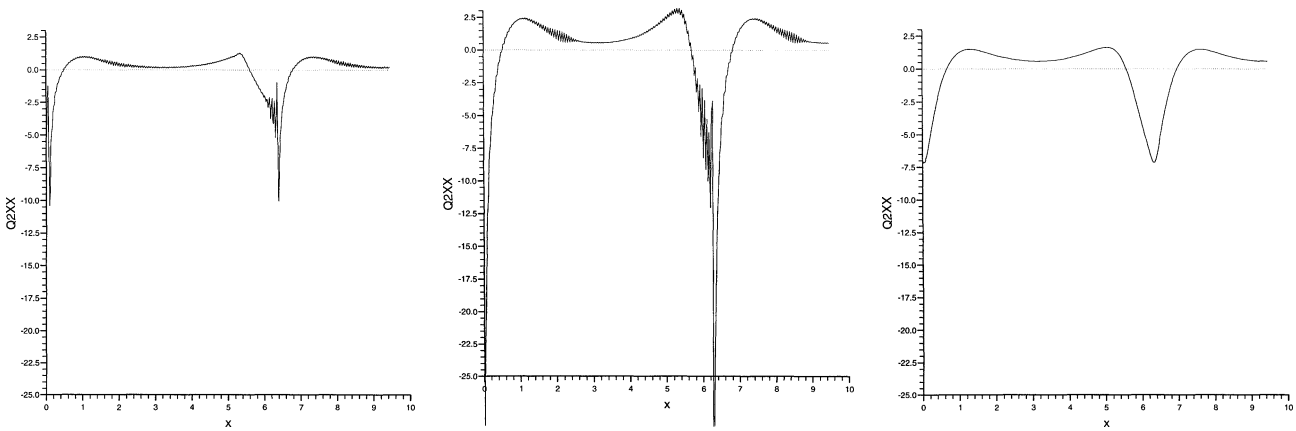

(b)

Figure 6. Computed solutions of (48) and (49) with nonzero $\bar{u}_1$ and/or F_1. (a) Compact-differencing results, with $r_1 = r_2 = 1, \bar{u}_1 = 1 - \exp(-y)$, for $B = 0$ on left (showing Q_{2x}) and $B = 125$ on right (showing Q_2). (b) Spectral results: left, $\bar{u}_1 = 100\ (1 - \exp(-y))$, $F_1 = 0$, $B = 0.25$, initial $\exp(-|k|)$; middle, $\bar{u}_1 = 0$, $F_{1k} = \exp(-k^2)$, $B = 25$, initial $3\exp(-|k|)$; right, as in middle but $B = 250$.

certain aspects of linear and nonlinear absolute and convective instability. Analytical properties have been studied, for the growth rates, profile curvature effects, nonlinear effects and so on, on a rational footing for undeveloped incident near-wake velocity profiles rather than on the basis of approximations at finite Reynolds numbers and/or arbitrary developed profiles; the wide variety of different near-wake profiles is described in Sections 1 and 2. The linear and nonlinear initial-value problems described in Sections 4–6 cover a range of quite general input disturbances in the near-wake, analogous with the work by Savin [41], Smith [42], Savin et al. [57] on onset transitions in surface-roughness flows. Nonuniform vorticity, even if comparatively small, as represented by the distortion profile $\bar{u}_1(y)$, can have a substantial impact on the linear disturbance evolution

in the near-wake, as negative (positive) profile curvature is found to be destabilising (stabilising), opposite to the response on a fixed surface. The response in the near-wake hinges on the function $y\bar{u}_1''$ in symmetric cases, and on an average in nonsymmetric ones, for the current setting. The implied destabilisation of the near-wake by a favourable basic pressure gradient (or stabilisation by an adverse gradient) acting ahead of the trailing edge is in contrast with the findings of Woodley and Peake [5] for more developed or fuller wake profiles, the contrast being due to different dynamics acting in our case over short length scales. It is intriguing that a delay of inviscid linear instability, to significant distances downstream of the trailing edge, could therefore be achieved by application of an adverse pressure gradient $\bar{p}'$ upstream of the trailing edge, provided that gradient is not too severe.

We should remark that the basic pressure gradient $\bar{p}'$ in the near-wake has little effect within the current short length scales, except insofar as it determines the influx B, whose nonlinear influence however is extremely important close to the trailing edge! The influx interacts with nonlinear effects in an interesting way, the type of nonlinear behaviour induced depending crucially on the input disturbance and its balance with B, as discussed in Sections 5 and 6. Examples in Sections 3 and 6, based on the typical near-wake profiles described in Sections 1 and 2, illustrate the presence of fairly strong local absolute or low-speed upstream or downstream convective instability for linear (due to $\bar{u}_1$) or nonlinear (due more to B, F_1) disturbances in the near-wake.

In particular, the nonlinear cases yield upstream-convecting disturbances as seen analytically in (51a,b) and numerically in *figures 5* and *6*. Increased initial amplitudes then are associated with increasing B values (increasing $\bar{p}'$), for a finite-time burst/transition (and for initial well-posedness), and so such amplitudes drive the typical bursting position ever closer to the tiny Navier–Stokes area at the trailing edge (see *figure 1*).

The underlined findings just above are the main ones of the paper and they hold for any sufficiently thin airfoil with attached flow.

A mixture of the input conditions considered in Sections 5 and 6 could be of interest, leading to a combination of the different nonlinear mechanisms operating there. The influence of the detailed flow features inside the Goldstein or Hakkinen–Rott viscous layers (Section 2) also needs to be incorporated for nonlinear disturbances of sufficiently shortened length scale. Similarly viscous forces enter play in the nonlinear critical layer(s) of Section 5 if the disturbance amplitude factor ε is related to an inverse power of the Reynolds number, adding terms $\propto \partial^2\hat{\tau}_1/\partial Y^2$ to the equation (37a); see references in Section 5. Second, the current approach for initial-value settings can be extended to three spatial dimensions; see Appendix A in the linear case and the Smith and Savin work for nonlinear three-dimensional disturbances. It would be further helpful to include nonparallel-flow effects and allow for trailing-edge geometry directly, cf. Hall and Smith [58], Merkin and Needham [59], Leib and Goldstein [60], Woodley and Peake [5], the last-named paper being corrected recently by Taylor and Peake [61], after completion of the current paper, incidentally. A similar extension is to include receptivity, for example for free-stream disturbances (Dr. D. Ashpis, private communication, 1997). Third, there may be a delicate interplay between the current inviscid instabilities and viscous instability of longer scale considered by F.T.S. with Prof. O.R. Burggraf in 1983 and later with Prof. D.T. Papageorgiou. Fourth, the present work tends to suggest a further examination of both the double-Blasius and the double Jobe–Burggraf sublayer profiles (see also *figure 2*) for absolute and convective instability, for their respective near wakes (models yield linear absolute or upstream convective instability but none is found yet for the particular double profiles just mentioned); likewise for other double profiles in the near-wake following an adverse or favourable pressure gradient upstream; and likewise for nonsymmetric double profiles, given the increased instability indicated by the averaging process of Sections 3.2 and 3.3. A small amount of reversed flow, say in $\bar{u}_1$, can have the same destabilising effect (Dr. L.S. Hultgren, private communication, 1997, and see details in earlier text and equations (B16), (14a), (16d)), while of course additional forward flow is stabilising. The present findings

of fairly strong instabilities in the near-wake for linear or nonlinear disturbances perhaps tend to call into question the relevance of studies on linear or nonlinear wake instability starting further downstream and in related flows. Finally, the extension to strongly nonlinear disturbances in a near-wake perhaps points to use of contour-dynamic computations (e.g., Clark and Johnson [38,39]) for the planar inviscid case if incident profile curvature is absent.

7.2. Comparisons

Comparisons with three-dimensional theory are presented in Appendix A.

Some helpful comparisons can also be made (*figure 7*) with the results of Hannemann and Oertel's [22] direct numerical simulations, granted that the latter results are for a thick (although not too thick) plate with a backward-facing step at the trailing edge rather than the thin trailing-edge configuration of current interest. The step induces reversed flow in the immediate wake; see a comment in the previous paragraph on the corresponding destabilising effect. Their Fig. 6 suggests a natural (nonlinear) frequency response ω_r of approximately 0.72, which is consistent with the other computed (linear) frequencies in their Figs. 16, 22. This frequency value then implies a typical shear value λ^+ of 0.72, according to the present theory (see our (11)), and, indeed, a profile slope of 0.72 (or $u \approx \lambda^+ y$) is in fair agreement with the direct-simulation profiles shown in their Fig. 11(a) (see our *figure 7*). Dritschel [36] also notes agreement with our (11) and the results of inviscid simulations, in the context of vortex dynamics. Further, Figs. 4, 7 of Hannemann and Oertel [22] point to a ratio of about 0.07 for the (nonlinear) growth rate ω_i over the frequency ω_r (see also their Fig. 16), a ratio which is in line with both the sign (negative) and smallness of the profile curvatures in their Fig. 11(a) (see our *figure 7*)(away from the centre-line) and the present theory based on $\varepsilon \bar{u}_1''$, with ε just below 0.1. Again, the nonlinear behaviour in their Fig. 6 indicates initial exponential growth of the (relatively small) mean-flow correction (their u_M) followed by saturation at later times (compare our Section 6); there are about 10 fast oscillations of u itself during a 50% change in their u_M, while the total change in u_M is near 10% of the maximum of u or $\partial u/\partial y$; and the typical fast time-scale $2\pi/\omega_r \approx 8.73$ suggests (from Section 6) a slow time of 87.3, of the order of the time variation in their Fig. 6; see our *figure 7*. These properties suggest a fair degree of agreement between the simulations and the theory. We should mention also the hint of a sawtooth response in their Fig. 8, compared with the current theoretical results in Section 6. This general agreement without short scales present is attributable to finite-Re effects.

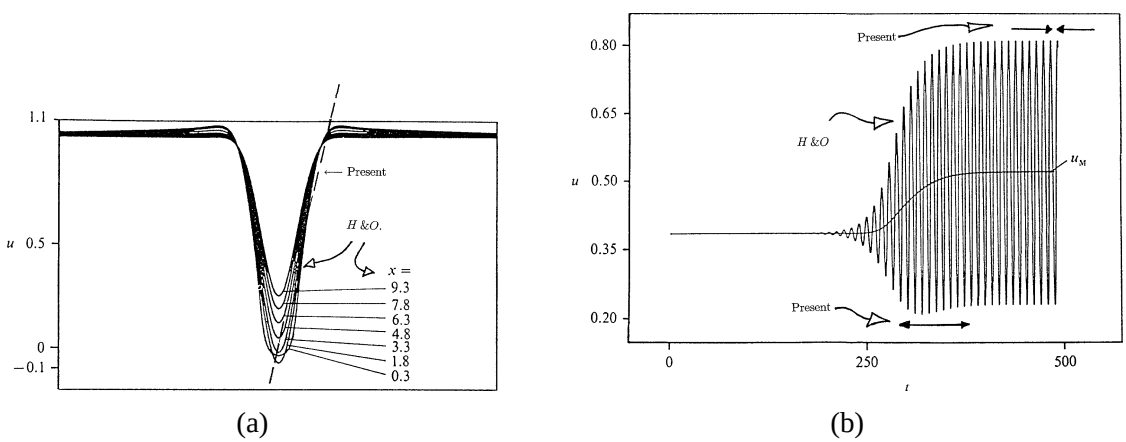

(a) (b)

Figure 7. Comparisons between present theory and direct simulations of Hannemann and Oertel [22], for the shear and the time scales.

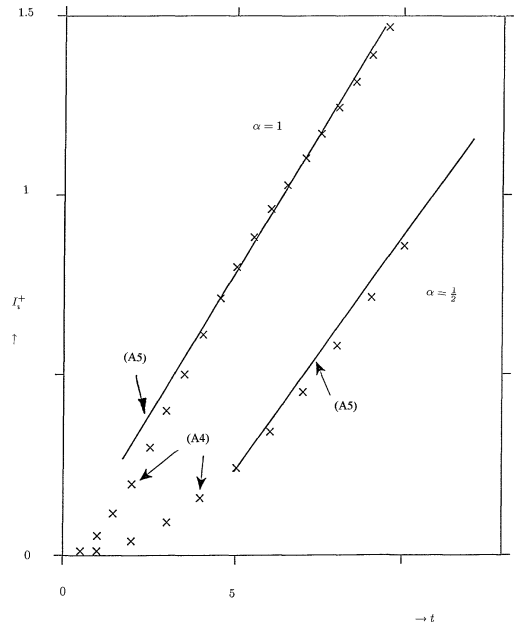

Figure 8. I_i^+ versus t for two values of α, from (A4), and comparison with (A5).

7.3. Further work

Further related work may also link the present results with numerical simulations on the modelling of turbulent structures and similar motions as mentioned in Section 1. The results on non-uniform vorticity, sublayer influx and nonlinearity may have particular significance there. The link with large-scale vorticity shedding of the von Karman form in the full wake is also of practical concern. Although the present frequency range is strictly higher than that associated with large-scale shedding, a liberal interpretation of the theoretical frequency $\frac{1}{2}[\partial u_D/\partial y_D]$ in dimensional terms from (11), (20), (43b) and Section 1 brings the two ranges together. It is interesting also that a combination of the basic nonuniform-vorticity and normal-influx flows (2) and (3) arises where the limitation (5d) is first relaxed, near the trailing edge, and a similar combination can arise within the exponentially decaying vorticity correction induced at a logarithmic normal distance outside the Hakkinen–Rott viscous layer. The latter vorticity correction, which is linearly stabilising, is linked closely with the stability properties of the Hakkinen–Rott- and Goldstein-layer profiles in *figures 1* and *2* and with the presence of an inflection point just outside each layer, in many near-wakes. There should be applications elsewhere as well, for instance to interfaces between different fluids (Bowles et al. [62]) and to breakaway separating motions at high Reynolds numbers (Vickers and Smith [63]). The latter motions contain local regions of near-uniform vorticity, albeit in the presence of a solid fixed surface, and they raise the possibility of pronounced absolute or upstream-downstream convective instability arising for linear or nonlinear general disturbances as in this work.

Appendix A. On two- and three-dimensional disturbances

For two-dimensional disturbances, we note first the basic examples $\exp(-x^2/4)$ and $2(1+x^2)^{-1}$ of initial conditions for ψ_0 or v_0 (say) at $t = 0$. These yield the respective solutions, for time $t \geqslant 0$, proportional to

$$\tfrac{1}{2}\left\{\pi^{1/2} + ix\int_0^1 e^{x^2s^2/4}\,\mathrm{d}s\right\}e^{-it-x^2/4} + \mathrm{CC}, \tag{A1}$$

$$2(\cos t + x\sin t)\left(1+x^2\right)^{-1}, \tag{A2}$$

at leading order, from (11), (19a)–(21e). In both cases the farfield response is therefore of a form $\propto x^{-1}\sin t$, giving slow algebraic decay. Second, on the influence of nonuniform vorticity in the temporal stage I, the Fourier transform of (27) gives, after integration with respect to t,

$$-2\gamma e^{i\alpha t/\gamma} f_{1t}^* = i\alpha d_0^* I^+, \tag{A3}$$

with

$$I^+ \equiv \int_0^\infty \frac{\bar{u}''(y)e^{-2\gamma y}}{(y-\gamma^{-1})}\left[\frac{y\left\{1-e^{-i\alpha t(y-\gamma^{-1})}\right\}}{i\alpha(y-\gamma^{-1})} - \frac{t}{\gamma}\right]\mathrm{d}y, \tag{A4}$$

in line with (14a)–(16d), (23)–(26b). For the example $\bar{u}_1'' = -\exp(-y)$ a numerical evaluation of the imaginary part of (A4) (using a substitution for $\alpha t(y-\gamma^{-1})$) is presented in *figure 8* at increasing t, for two representative values of α. The large-t asymptote, from analysis of (A4), is

$$I_i^+ \sim -\left[\frac{\bar{u}_1''(\gamma^{-1})\pi}{\alpha e^2}\right]t, \tag{A5}$$

which is also shown in the figure for comparison, indicating fair agreement for times t beyond about 4. Here (A5) predicts only the slope at large t in effect and so a permissible origin shift in t is included in the plotting of (A5) in the figure. Further, the result (A5) confirms the linear growth of f_1 at large t which is mentioned just after (28c) and is consistent with the growth rate (15).

For three-dimensional disturbances, the simple dispersion relation (11) holding at leading order is replaced by $\omega_0 = \alpha/(\alpha^2+\beta^2)^{1/2}$ where β is the spanwise (z) wavenumber. Hence the leading-order behaviour itself becomes more complicated, giving the typical disturbance solution

$$4\pi^2 Q(x,z,t) = \int_{-\infty}^{\infty}\int_{-\infty}^{\infty} Q^*(\alpha,\beta)\exp\left[i\left\{\alpha x + \beta z - \frac{\alpha t}{(\alpha^2+\beta^2)^{1/2}}\right\}\right]\mathrm{d}\alpha\,\mathrm{d}\beta \tag{A6}$$

in terms of an initial Fourier transform $Q^*(\alpha,\beta)$, cf. (20). An example is for $Q^* = \exp(-\sigma(\alpha^2+\beta^2)^{1/2})$ which corresponds to a radially symmetric input Q equal to $(\sigma/2\pi)(r^2+\sigma^2)^{-3/2}$ at $t=0$, with σ being a positive constant. Switching to polar coordinates $(\alpha,\beta) = R(\cos\phi,\ \sin\phi)$ then allows integration in R, leaving

$$4\pi^2 Q = \int_0^{2\pi}\frac{\exp(-it\cos\phi)\,\mathrm{d}\phi}{[\sigma - ir\cos(\theta-\phi)]^2}, \tag{A7}$$

where $(x,z) = r(\cos\theta,\ \sin\theta)$. Solution contours at various times t are presented in *figure 9*(*a*). They demonstrate the fore-aft symmetry present here, the solution being even in x and in z. It is noticable also as t increases that there appears to be a near-planar response persisting near the origin of the disturbance, but nevertheless the maximum amplitude arises in a direction slightly inclined from the z-axis, and further some disturbance activity travels upstream and downstream. These features tie in with the large-time asymptotes.

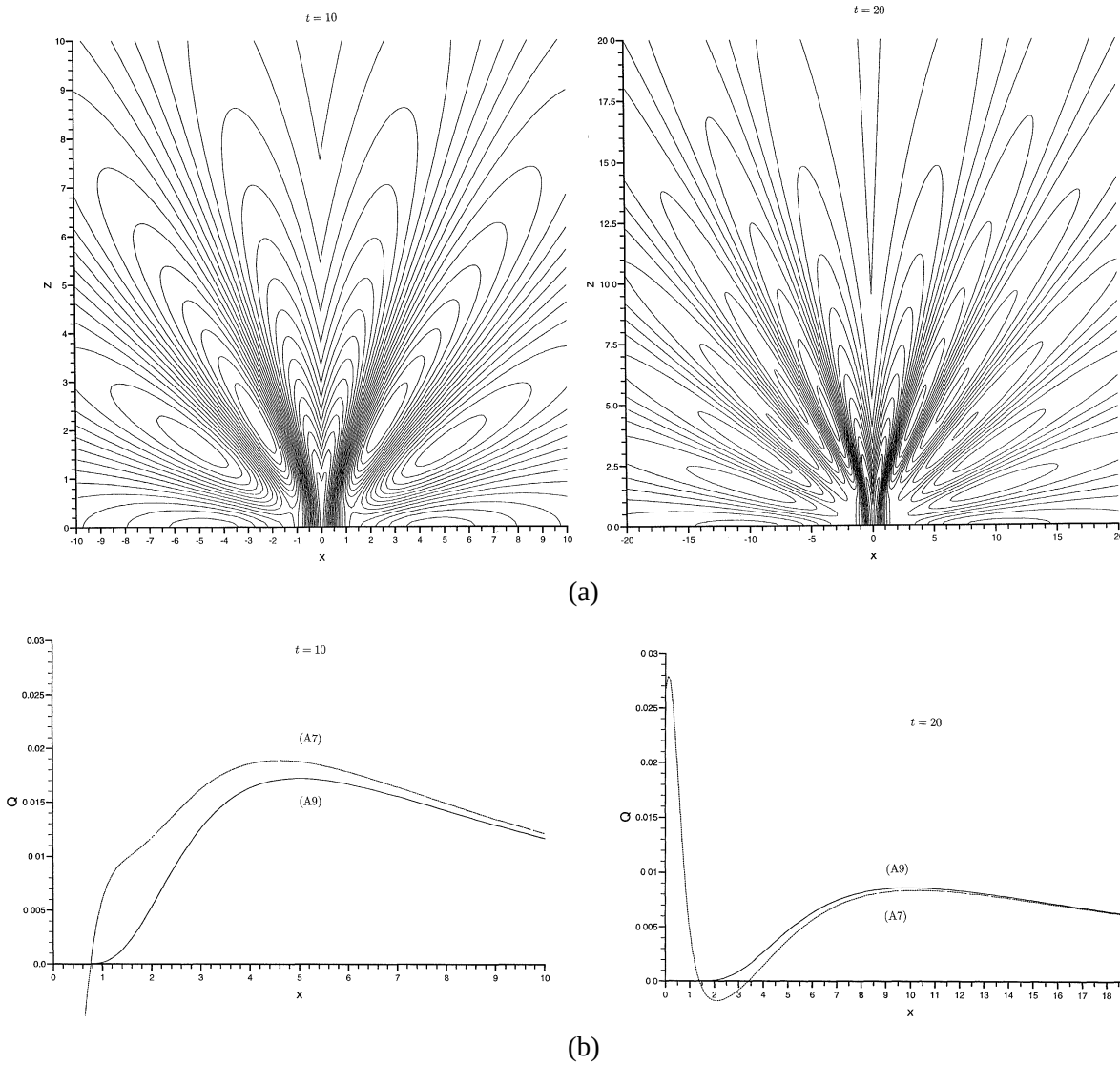

Figure 9. Three-dimensional disturbances. (a) Solution contours for (A7); $t = 10,\ 20$, contour levels -0.04 (0.0025) 0.03. (b) Comparison between (A9) and (A7) along $z = 0$ at times $t = 10,\ 20$.

Thus, for x of O(1) but z large of O($t^{1/2}$), (A7) gives

$$4\pi^2 Q \sim \frac{e^{-it}}{t^{1/2}} \int_{-\infty}^{\infty} \frac{\exp(i\hat{\phi}^2/2)\,\mathrm{d}\hat{\phi}}{[\sigma - i(x + \hat{z}\hat{\phi})]^2} \tag{A8}$$

for $t \gg 1$, with $z = t^{1/2}\hat{z}$. By contrast, far downstream (and similarly far upstream) there is a corridor of significant amplitude variation wherein $x \sim t$ but $z \sim 1$, such that

$$\pi Q \sim \frac{\exp(i\tilde{\theta} - \sigma/\tilde{r})}{t\tilde{r}^2} \tag{A9}$$

when $t \gg 1$. Here $\tilde{\theta} \equiv t\theta$, $\tilde{r} \equiv t^{-1}r$ are of O(1). Both (A8), (A9) are in fair agreement with the solution (A7) as time increases, the comparison in *figure 9*(*b*) confirming this for the region of validity of (A9). Clearly the main amplitude variation is confined to the O(1) neighbourhood of the origin, as in (A8), which shows that a fixed- frequency response does occur in this 3D case but with slow amplitude decay $\propto t^{-1/2}$, as distinct from the fixed amplitude of the 2D case in (A1), (A2) for instance. In fact the solution (A7), at the origin $r = 0$, yields $2\pi\sigma^2 Q = J_0(t)$ for all t, where J_0 is the zeroth-order Bessel function, and this likewise gives the $t^{-1/2}$ amplitude decay. Also, (A8) verifies the existence of a region of quasi-planar behaviour near the origin at large times. The critical-layer behaviour in this 3D case with nonuniform vorticity and/or nonlinearity could be very interesting, and likewise for the influence of slight three-dimensionality during the second temporal stage.

Appendix B. Examples for Section 3.3

Given the many different near-wake profiles noted in Sections 1 and 2, we consider profiles of symmetric type first. If $\bar{u}_1'' = -\bar{k}y^{-N}$ for $y > \bar{a}_1$, with $\bar{k}, \bar{a}_1, N$ positive real constants, then formally $g_1 \to \bar{k}\pi e^{-2}\alpha^{N-1}$ for small $\bar{a}_1$. The response of g_2 is less simple but the linear dependence of g_1 on α when $N = 2$ suggests strong temporal growth in (16b). For instance if $\hat{q}^*(\alpha) \propto \exp(-\sigma\alpha)$ with σ a positive real constant, corresponding to an algebraically decaying initial disturbance $\propto (\sigma^2 + x^2)^{-1}$, then the implication is that the disturbance amplitude tends to infinity at the finite positive time $T = \alpha e^2 \pi^{-1}\bar{k}^{-1}$ for any x position. Similarly strong growth is suggested when $N = 1$, yielding $\exp(\pi e^{-2}\bar{k}T)$ dependence at all x positions. Both of these cases correspond to high-curvature instability near the centre-line where $y\bar{u}_1''$ is large and negative. Although each profile is irregular there in fact the implied large growth at large negative $y\bar{u}_1''$ values is borne out by the analysis below. When N is zero or -1, on the other hand, and $\bar{a}_1$ becomes large, the maximal growth rates do not occur in the current region where y is of O(1) and instead are likely to arise further out where the full original boundary-layer profile takes effect as in Papageorgiou and Smith [4], corresponding to smaller wavenumbers and hence smaller growth rates.

The influence of high negative $y\bar{u}_1''$ values implied above may be observed clearly in cases where $-y\bar{u}_1''$ has an enhanced local maximum at a nonzero $y = y_0$, of the form

$$-\bar{u}_1''(y) \sim \ell^{-1}F(Y) \quad \text{for } y - y_0 = \ell Y \tag{B1}$$

with ℓ small and positive and F, Y of O(1). Here strictly ℓ is supposed to remain much greater than ε in order to preserve the flow structure assumed in Subsection 3.2. Then (16c,d) suggest examining the solution near $\alpha y_0 = 1$, giving the complex frequency

$$\Omega \sim \left(\frac{\pi y_0}{e^2\ell}\right)\left\{\frac{(FP)}{\pi} - \int_{-\infty}^{\infty}\frac{F(Y)\,\mathrm{d}Y}{(Y-\beta)} + iF(\beta)\right\}, \tag{B2}$$

where $\alpha = y_0^{-1} - \ell y_0^{-2}\beta$ with β real and FP denotes the finite part of the integral. The additional contribution to Ω from the last term of (16d) is $\bar{u}_1(0)/y_0$, which is taken to be small compared with (B2). Thus large growth rates of order ℓ^{-1} are to be expected here. Moreover the form of the term in curly brackets shows it to be the value of a complex analytic function $\mathcal{F}$ of β, evaluated as $\beta_i \to 0+$ say, in general. So numerous cases suggest themselves. Some relevant examples of local profile curvature shapes are, with a_{1r}, a_2, a_3, a_4 being positive real constants,

$$F(Y) = a_{1r} - a_2(Y^2 - 1), \tag{B3}$$

$$F(Y) = \{2Y + a_3(2 - Y^2)\}\{(2 - Y^2)^2 + 4Y^2\}^{-1}, \tag{B4}$$

$$F(Y) = a_4\{(1 + Y^2)^{-1} + 2(4 + Y^2)^{-1}\}, \tag{B5}$$

$$F(Y) = 1 + Y \text{ for } Y < 0,\ Y \text{ for } Y > 0. \tag{B6}$$

These exhibit in turn a local positive maximum in the negative curvature $-\bar{u}_1''$, a local maximum and minimum (e.g. if a_3 is small) with Y^{-2} decay at large $|Y|$, a local maximum with Y^{-2} decay, and a local discontinuity at a maximum. The corresponding complex functions $\mathcal{F}$ show the maximal complex growth rates and wavenumbers to be given by

$$\left(\frac{e^2\ell}{\pi y_0}\right)\Omega_{\max} = \begin{cases} ia_{1r} - a_{1i}, \\ 1 + ia_3, \\ \mp 2a_4, \\ -\frac{1}{\pi}(1 + \ell n(\pi b_0)) - a_5, \end{cases} \qquad \beta_{\max} = \begin{cases} i, \\ -i, \\ (\pm 1 - 3i)/2, \\ \pi^{-1}b_0^{-1}, \end{cases} \tag{B7–B10}$$

respectively, where $b_0 = a_0 - i$ and a_{1i}, a_5, a_0 are real constants. These results confirm in (B7)–(B10) the presence of large local maxima (saddle points) of the scaled complex frequency Ω in the complex β plane, with Ω_i positive, and hence, from the method of continuous contour deformation and steepest descents, large exponential disturbance growth in T from (16a–d), specifically at the central location $x = 0$. They also merge with the growth results inferred for $N = 1, 2$ in the previous paragraph. In the cases of (B4)–(B6) there are in addition poles or a branch cut present in the complex β plane but these have less effect on the disturbance growth than do the extrema (B7)–(B10).

The local maxima in (B1)–(B10) can also induce a significant non-local effect by means of their influence as delta functions when viewed on the y-scale of O(1). This is particularly relevant to profiles of nonsymmetric type in view of the average combination/addition mentioned earlier in this subsection for such profiles. Consider for instance the curvature profile $\bar{u}_1'' = -\exp(-y)$. This yields a maximum of $g_1(\alpha)$ along the real axis at $\alpha = 1$ according to (16c), but from (16d) $g_2(\alpha)$ there is not maximal in general, having slope $\mathrm{d}g_2/\mathrm{d}\alpha = -\bar{b}$ $-\bar{u}_1(0)$where $\bar{b} = 1/3$; see *figure 3*. If there is an additional strong local variation $\hat{\lambda}_0\delta(y - y_0)$ in $-\bar{u}_1''(y)$ at $y = y_0$, proportional to a delta function, then that adds (from (16d))

$$-\hat{\lambda}_0 \exp(-2\alpha y_0)(\alpha y_0 - 1)^{-1} \tag{B11}$$

to $g_2(\alpha)$ while leaving $g_1(\alpha)$ unaffected for $\alpha y_0 \neq 1$. Here $\hat{\lambda}_0$, y_0 are positive real constants, and the dependence in (B11) is observed to match with that in (B1)–(B4), (B8) near $\alpha = y_0^{-1}$. It follows that the combined slope $\mathrm{d}g_2/\mathrm{d}\alpha$ at $\alpha = 1$ is then

$$\hat{\lambda}_0 y_0(2y_0 - 1)(y_0 - 1)^{-2}\exp(-2y_0) - \bar{b} - \bar{u}_1(0), \tag{B12}$$

for $y_0 \neq 1$. So there are two roots y_0 for which g_2 as well as g_1, and hence Ω (complex), is maximal at $\alpha = 1$; otherwise the local complex maximum of Ω occurs at a complex value of α. If the strength factor $\hat{\lambda}_0$ is relatively large one such root has $y_0 \to 1/2$, from (B12). This additional non-local effect applies quite generally to other curvature profiles which decay sufficiently rapidly at large y. A related non-local effect arises from a variation $\hat{\mu}_0\delta(y - y_0)$ in the distortion shear $-\bar{u}_1'$, with $\hat{\mu}_0$ a real constant, which gives

$$g_2(\alpha) = \alpha\hat{\mu}_0 \exp(-2\alpha y_0)(1 - 2\alpha y_0)(\alpha y_0 - 1)^{-2} \tag{B13}$$

for $\alpha \neq y_0^{-1}$. This matches with (B5) as $\alpha \to y_0^{-1}$, but its real maximum is at $\alpha = (3y_0)^{-1}$ and it can be combined with a negative decaying curvature profile $\bar{u}_1''(y)$ such as $-\exp(-y)$ as before to induce a complex maximum in Ω at a real or a complex value of α. Similar combinations yielding maximal Ω values with positive Ω_i are obtained by involving (B7)–(B10). Again, two delta functions in $\bar{u}_1''$ centred at $y = y_0, y_1$ with strength factors $\hat{\lambda}_0, \hat{\lambda}_1$ respectively combine as

$$g_2(\alpha) = \frac{\hat{\lambda}_0 e^{-2z}}{(z-1)} + \frac{\hat{\lambda}_1 e^{-2\upsilon z}}{(\upsilon z - 1)} - \alpha \bar{u}_1(0), \tag{B14}$$

where $z = \alpha y_0 (\neq 1, \upsilon^{-1})$, $\upsilon = y_1/y_0$. Hence extrema occur where

$$\hat{\lambda}_0(2z-1)(\upsilon z - 1)^2 = -\hat{\lambda}_1(2\upsilon z - 1)\upsilon(z-1)^2 e^{2(1-\upsilon)z} \tag{B15}$$

in the case of zero $\bar{u}_1(0)$. If $\upsilon = 2$ and $\hat{\lambda}_1$ is small for example then there are extrema at $2z \approx 1 + [\hat{\lambda}_1/(2\hat{\lambda}_0 e)]^{1/3} z_1$ from (B15), with z_1 equal to -1, to $\exp(i\pi/3)$ or to its complex conjugate. One of the latter two values of z_1 therefore leaves Ω_i being positive.

We conclude, then, that the maximal wavenumbers α may be real or complex, depending on the $\bar{u}_1(y)$ profile, as in (B7)–(B10) and (B11)–(B15). The majority of the examples here show that the near-wake flow can be absolutely unstable locally, for instance from the large-T exponential behaviour of (16a,b) at the central input location $x = 0$, given the maxima in (B7)–(B10), (B11)–(B15). Other examples show only convective instability, although with strong growth rates again and with comparatively small convection speeds in view of the low typical velocities involved locally. Again, slight flow reversal, corresponding to a decrease of $\bar{u}_1$ by a constant $\bar{u}_{1r}$ say, effectively subtracts $\alpha \bar{u}_{1r}$ from ω_1 or from $-g_2$ (see (14a) and (16d)), e.g. in (14a) and *figure 3*, and so it readily provokes absolute instability; the necessary value for this in the case of *figure 3* is $\bar{u}_{1r} = \bar{b}$, i.e. decrease $\bar{u}$ by the amount $\varepsilon \bar{b}$. Hence, in particular, local linear absolute instability is predicted for the near-wake profile

$$\bar{u} = |y| + \varepsilon\left[1 - \exp(-|y|) - \bar{b}\right], \tag{B16}$$

with $\bar{b} = 1/3$, for the real maximal wavenumber $\alpha = 1$; compare the results for double-Jobe–Burggraf profiles in *figure 2*. By the same token, (14a) shows explicitly that the addition of slight forward flow tends to alter upstream convective instability towards absolute or downstream convective instability. In general, the implied slow-time amplitude growth

$$\exp(g_1 T), \quad \text{where } g_1 = \Omega_i, \tag{B17}$$

from (B7)–(B10) for instance, or from (B16), is the dominant disturbance growth since at leading order the response is one of constant-frequency oscillation, as indeed is indicated in (16a,b).

Acknowledgements

Helpful comments by Dr. T. Allen, Dr. D. Ashpis, Dr. R.I. Bowles, Prof. S.N. Brown, Dr. S.R. Clarke, Dr. L.S. Hultgren, Prof. E.R. Johnson, Dr. A. Jones, Dr. N. Peake, Dr. N. Sandham, Prof. J.T. Stuart, Dr. S.N. Timoshin and the referees are gratefully acknowledged, as is support from the EPSRC Mathematics Programme and MOD, UK.

References

[1] Drazin P.G., Howard L.N., Adv. Appl. Mech. 9 (1966) 1–89.
[2] Mattingly G.E., Criminale W.O., J. Fluid Mech. 51 (1972) 233–272.
[3] Drazin P.G., Reid W.H., Hydrodynamic Stability, Cambridge University Press, 1981.
[4] Papageorgiou D.T., Smith F.T., J. Fluid Mech. 208 (1989) 67–89.
[5] Woodley B.M., Peake N., J. Fluid Mech. 339 (1997) 239–260.
[6] Sato J., Kuriki K., J. Fluid Mech. 11 (1961) 321–352.
[7] Miksad R.W., Jones F.L., Kim Y.C., Khandra L., J. Fluid Mech. 123 (1982) 1–29.
[8] Miksad R.W., Jones F.L., Powers E.J., Phys. Fluids 26 (1983) 1402–1409.
[9] Gaster M., Phys. Fluids 11 (1968) 723–727.
[10] Gaster M., ARC R. and M. (1969) 3595.
[11] Gaster M., Proc. Workshop on transition, ICASE, NASA Langley, VA, U.S.A., 1991.
[12] Huerre P., Monkewitz P.A., Annu. Rev. Fluid Mech. 22 (1990) 473–537.
[13] Monkewitz P.A., Huerre P., Chomaz J.M., J. Fluid Mech. 251 (1993) 1–20.
[14] Allen T., Riley N., Aeronaut. J. (Dec.) (1995) 439–448.
[15] Lingwood R.J., J. Fluid Mech. 331 (1996) 405–428.
[16] Drazin P.G., Quart. J. Mech. Appl. Math. 27 (1974) 69–86.
[17] Le Dizès S., Huerr, P., Chomaz J.M., Monkewitz P.A., Philos. T. Roy. Soc. A 354 (1996) 169–212.
[18] Papageorgiou D.T., Smith F.T., P. Roy. Soc. A Lond. 419 (1988) 1–28.
[19] Goldstein M.E., Hultgren L.S., J. Fluid Mech. 197 (1988) 295–330.
[20] Goldstein M.E., Choi S.-W., J. Fluid Mech. 207 (1989) 97–120.
[21] Goldstein M.E., Choi S.-W., J. Fluid Mech. 216 (1990) 659–663.
[22] Hannemann, Oertel, J. Fluid Mech. 199 (1989) 55–88.
[23] Jackson C.P., J. Fluid Mech. 182 (1987) 23–45.
[24] Goldstein S., Proc. Camb. Phil. Soc. 26 (1930) 1–30.
[25] Hakkinen R.J., Rott N., AIAA J. 3 (1965) 1553.
[26] Stewartson K. Mathematika 16 (1969) 106.
[27] Messiter A.F., SIAM J. Appl. Math. 18 (1970) 241.
[28] Jobe C.E., Burggraf O.R., P. Roy. Soc. Lond. A 340 (1974) 91–111.
[29] Chow R., Melnik R.E., Proc. 5th Int. Conf. Num. Meth. Fluid Dyn., Enschede, The Netherlands 59 (1976) 135–144.
[30] Veldman A.E.P., van de Vooren A.I., Lec. Notes in Phys., Berlin, Springer-Verlag, Vol. 35, 1976, p. 422.
[31] Smith F.T., J. Fluid Mech. 131 (1983) 218–249.
[32] Smith F.T., Timoshin S.N., P. Roy. Soc. Lond. A 452 (1996) 1301–1329.
[33] Smith F.T., Timoshin S.N., J. Fluid Mech. 324 (1996) 355–377.
[34] Bowles R.G.A., Smith F.T., Q. J. Mech. Appl. Math. (1999) (accepted for publication).
[35] Dritschel D., J. Fluid Mech. 172 (1986) 157–182.
[36] Dritschel D., J. Fluid Mech. 194 (1988) 511–547.
[37] Pullin D.J., Jacobs P.A., Grimshaw R.H.J., Saffman P.G., J. Fluid Mech. 209 (1989) 359–384.
[38] Clarke S.R., Johnson E.R., J. Fluid Mech. 343 (1997) 131–151.
[39] Clarke S.R., Johnson E.R., J. Fluid Mech. 343 (1997) 153–168.
[40] Kawahara G., Kida S., Tanaka M., Yanese S., Phys. Fluids (1996) (submitted).
[41] Savin D.J., Ph.D. thesis, University London, 1996.
[42] Smith F.T., AIAA paper 96-1992, New Orleans meeting, June, 1996.
[43] Elliott J.W., Smith F.T., Comput. Fluids 14 (2) (1986) 109–116.
[44] Hocking L.M., Q. J. Mech. Appl. Math. 28 (1975) 341–353.
[45] Stewartson K., Math. Models and Methods in Mechs., Banach Cent. Pubs. 15 (1985) 679–725.
[46] Stewartson K., IMA J. Appl. Math. 27 (1981) 133–175.
[47] Veldman A.E.P., Report TW-157, Mathematisch Inst., Rijksuniv, Groningen, The Netherlands, 1975.
[48] Benney D.J., Bergeron R.E., Stud. Appl. Math. 48 (1969) 191–204.
[49] Haberman R., Stud. Appl. Math. 51 (1972) 139–161.
[50] Stewartson K., Geophys. Astro. Fluid 9 (1978) 185–200.
[51] Hickernell F.J., J. Fluid Mech. 42 (1984) 431–449.
[52] Gajjar J.S.B., Smith, F.T., J. Fluid Mech. 157 (1985) 53–77.
[53] Goldstein M.E., Leib S.J., J. Fluid Mech. 191 (1988) 481–515.
[54] Brown S.N., Stewartson K., Geophys. Astro. Fluid 10 (1978) 1–24.
[55] Warn T., Warn H., Stud. Appl. Math. 59 (1978) 37–71.
[56] Li L., Walker J.D.A., Bowles R.I., Smith, F.T., J. Fluid Mech. 374 (1998) 335–378.
[57] Savin D.J., Smith F.T., Allen T., P. Roy. Soc. Lond. A 455 (1999) 491–541.

[58] Hall P., Smith F.T., Stud. Appl. Math. (1984).
[59] Merkin J.H., Needham D.J., Q. J. Mech. Appl. Math. 40 (1981) 559–574.
[60] Leib S.J., Goldstein M.E., J. Fluid Mech. 168 (1986) 479–500.
[61] Taylor M.J., Peake N., Eur. J. Mech. B-Fluids 18 (4) (1999) 573–579.
[62] Bowles R.I., Caporn P., Timoshin S.N., P. Roy. Soc. Lond. A 454 (1998) 3223–3256.
[63] Vickers I.P., Smith F.T., J. Fluid Mech. 268 (1994) 147–173.